Molecular Systems Biology 4; Article number 186; doi:10.1038/msb.2008.23
Citation: ***Molecular Systems Biology*** **4:186**

www.molecularsystemsbiology.com

molecular systems biology

Reverse engineering of force integration during mitosis in the *Drosophila* embryo

Roy Wollman[1,2,*], Gul Civelekoglu-Scholey[1,2], Jonathan M Scholey[1,2] and Alex Mogilner[1,3,4]

[1] Laboratory of Cell and Computational Biology, Center for Genetics and Development, University of California at Davis, Davis, CA, USA, [2] Department of Molecular and Cell Biology, University of California at Davis, Davis, CA, USA, [3] Department of Neurobiology, Physiology and Behavior, University of California at Davis, Davis, CA, USA and [4] Department of Mathematics, University of California at Davis, Davis, CA, USA

* Corresponding author. Department of Molecular and Cellular Biology, University of California at Davis, 1 Shields Ave., Davis, CA 95616, USA. Tel.: +1 530 752 2273; Fax: +1 530 732 7522; E-mail: rwollman@ucdavis.edu

Received 5.10.07; accepted 7.3.08

The mitotic spindle is a complex macromolecular machine that coordinates accurate chromosome segregation. The spindle accomplishes its function using forces generated by microtubules (MTs) and multiple molecular motors, but how these forces are integrated remains unclear, since the temporal activation profiles and the mechanical characteristics of the relevant motors are largely unknown. Here, we developed a computational search algorithm that uses experimental measurements to 'reverse engineer' molecular mechanical machines. Our algorithm uses measurements of length time series for wild-type and experimentally perturbed spindles to identify mechanistic models for coordination of the mitotic force generators in *Drosophila* embryo spindles. The search eliminated thousands of possible models and identified six distinct strategies for MT–motor integration that agree with available data. Many features of these six predicted strategies are conserved, including a persistent kinesin-5-driven sliding filament mechanism combined with the anaphase B-specific inhibition of a kinesin-13 MT depolymerase on spindle poles. Such conserved features allow predictions of force–velocity characteristics and activation–deactivation profiles of key mitotic motors. Identified differences among the six predicted strategies regarding the mechanisms of prometaphase and anaphase spindle elongation suggest future experiments.
Molecular Systems Biology 29 April 2008; doi:10.1038/msb.2008.23
Subject Categories: computational methods; cell cycle
Keywords: genetic algorithm; mathematical model; mitosis; reverse engineering; spindle

Introduction

Mitosis, the process by which identical copies of the replicated genome are distributed to the products of each cell division, involves a highly dynamic sequence of coordinated motility events mediated by a bipolar mitotic spindle (Karsenti and Vernos, 2001; Pines and Rieder, 2001; Scholey *et al*, 2003) (Figure 1A). The motility is driven by forces generated by multiple molecular motors—kinesins and dyneins—together with dynamic microtubules (MTs) (Figure 1B) (Kline-Smith and Walczak, 2004; Brust-Mascher and Scholey, 2007) whose activities are controlled by kinases, phosphatases and proteases (O'Farrell, 2001; Parry and O'Farrell, 2001; Peters, 2002). These force-generating and regulatory proteins form a vast network that coordinates spindle assembly, maintenance and elongation, as well as orchestrating chromosome segregation.

In the *Drosophila* syncytial embryo, hundreds of mitotic spindles progress synchronously through a well-defined and reproducible sequence of transitions, in which periods of rapid pole–pole separation are interspersed with quiescent pauses (Sharp *et al*, 2000a). Each mitosis begins with prophase when the centrosomes located on the nuclear envelope separate with roughly hyperbolic kinetics to reach a steady-state separation distance of about 6–8 μm. Then following nuclear envelope breakdown at the onset of prometaphase, the spindle elongates further to reach another steady-state length of 10 μm in metaphase. Sister-chromatid segregation occurs during anaphase A and then the spindle undergoes a final linear episode of elongation to reach a final length of 14 μm in anaphase B (Sharp *et al*, 2000b; Brust-Mascher and Scholey, 2002).

Mitotic spindle dynamics depends upon the combined effect of several distinct molecular processes including, for example, force-generating mechanisms, changes in the concentration of MT components, the presence or absence of centrosomes, the establishment of morphogen gradients, etc. (Sharp *et al*,

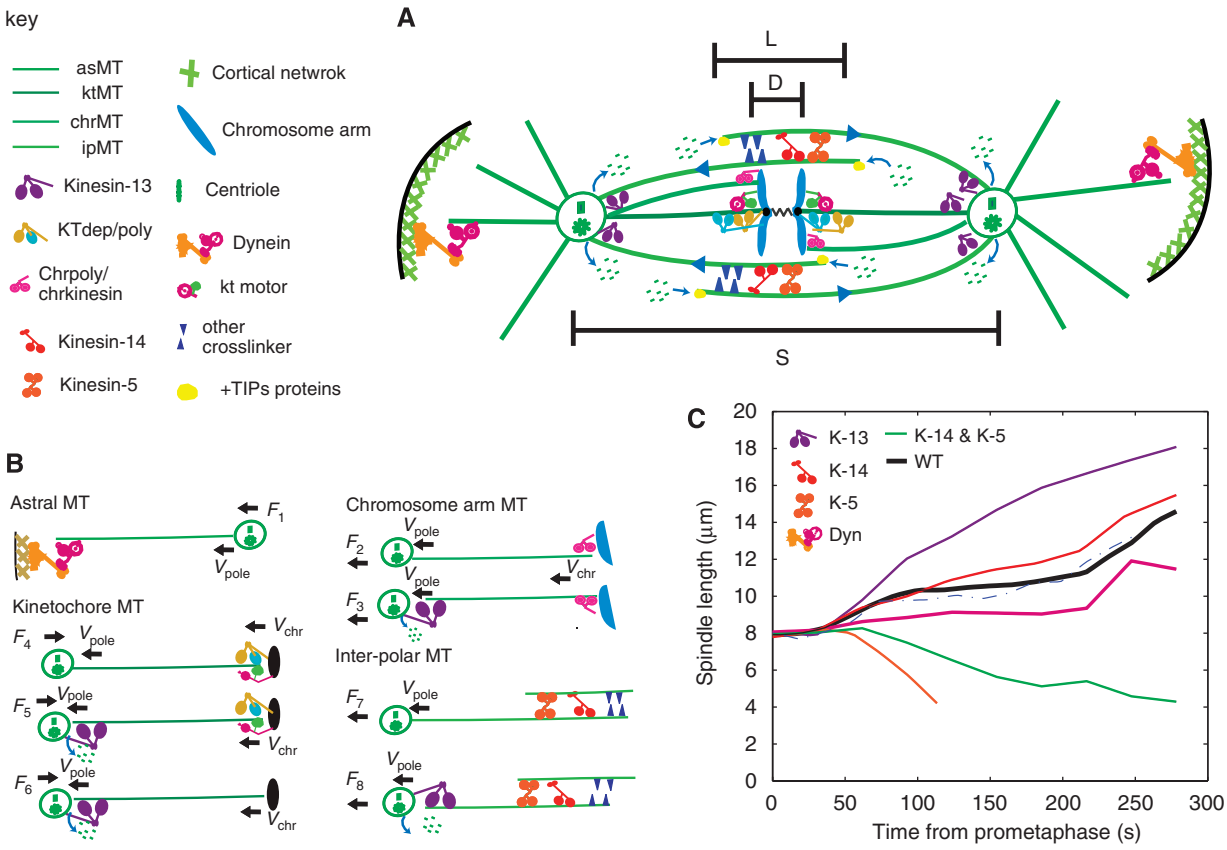

Figure 1 The spindle protein machinery. (**A**) A cartoon that shows all major components of the spindle. Four MT populations (astral (as), kinetochore (kt), chromosome arm (chr) and inter-polar (ip) MTs) extend from the poles creating the spindle. Molecular motors bind to MTs and either regulate their ends' kinetics, or slide them, or exert forces on the chromosomes and centrosomes. (**B**) Eight possible MT–motor combinations, with the respective velocities and forces acting on a single MT. *asMT:* cortical dynein pulling the MT generates an outward force F_1 on the spindle pole. *chrMT* are anchored at the pole, while MT polymerization and chromokinesins generate a pushing force F_2; a force F_3 is associated with such an MT if depolymerases are activated at the MT's minus end in addition to motor activity at the MT's plus end. *ktMT:* an inward force, F_4 is generated on an MT anchored at the pole while kt motors act on the MT plus end; modified force F_5 acts on an MT depolymerized at the minus end in addition to the plus end motor activity; force F_6 is exerted if ktMT is depolymerized at its minus end and anchored at its plus end. *ipMT:* an outward force, F_7 results from the combination of kinesin-5 and kinesin-14 actions on the MT anchored at the pole, while a force F_8 is exerted by these motors on an MT being depolymerized at its minus end. (**C**) The experimentally measured time series for spindle length (pole–pole distance) in wild type (WT) and inhibited spindles used in the optimization process (details in Supplementary Figure 1, referenced in Supplementary Table 2). Colors correspond to motor colors in the legend. Previous studies revealed that the double inhibition of kinesin-5 and kinesin-14 fully rescues metaphase spindle assembly (dashed blue line, not used here) (Sharp *et al*, 2000b). However, recent studies suggest that this effect results from the partial inhibition of kinesin-5, whereas a more complete inhibition leads to prometaphase spindle collapse even in kinesin-14 null mutants (green line, used here), suggesting that an additional unknown inward force also opposes kinesin-5 and contributes to the collapse (Brust-Mascher and Scholey, in preparation).

2000a; Karsenti and Vernos, 2001; Mitchison and Salmon, 2001; Mitchison *et al*, 2005). The extent to which these distinct processes influence mitotic spindle behavior appears to differ in different systems. However, the important idea that balances of antagonistic forces contribute to mitosis is thought to apply to a broad range of mitotic spindles. This idea was originally proposed by Ostergren (1951) to explain chromosome positioning and provided a plausible explanation for spindle pole dynamics in experimentally perturbed diatom spindles (Leslie and Pickett-Heaps, 1983). On the basis of observations of interactions among mutant genes encoding members of the yeast kinesin-5 and kinesin-14 families (Lawrence *et al*, 2004), it was proposed that the corresponding motor proteins could exert antagonistic outward and inward forces on spindle poles, respectively (Saunders and Hoyt, 1992; Hoyt and Geiser, 1996). The idea that these counter-balancing forces are generated by an 'antagonistic sliding filament mechanism' was supported by biochemical studies showing that purified kinesin-5 is a slow, plus-end-directed bipolar homotetramer capable of crosslinking and sliding apart antiparallel MTs, whereas kinesin-14 is a minus-end-directed homodimeric MT bundling motor that could slide antiparallel MTs inwards (McDonald *et al*, 1990; Walker *et al*, 1990; Sawin *et al*, 1992; Cole *et al*, 1994; Kashina *et al*, 1996; Kapitein *et al*, 2005; Oladipo *et al*, 2007; Furuta and Toyoshima, 2008). The hypothesis that pole–pole separation depends upon a balance of forces generated by such an antagonistic sliding filament mechanism is further supported by observations that purified kinesin-5 and kinesin-14 can antagonize and balance one another in motility assays (Tao *et al*, 2006), although further work is needed to establish if and how this mechanism contributes to spindle pole dynamics.

In the *Drosophila* syncytial embryo, a motor-generated force balance produced by systems of complementary and antagonistic motors is proposed to play a dominant role in spindle assembly/elongation and chromosome segregation (Sharp *et al*, 2000b). For example, comparison of the temporal changes in *Drosophila* embryo spindle length in five mutant and biochemically inhibited spindles reveals characteristic defects in pole–pole separation compared to wild-type (WT) spindles. Each defect can be most naturally explained by a shifting force balance in the spindle resulting from the inhibition of specific molecular motors (Figure 1C). For example, when either dynein or kinesin-5, presumably pulling the astral (as) MTs outward or sliding the inter-polar (ip) MTs outward, respectively, are inhibited, spindle length decreases. On the other hand, both kinesin-13 and -14 are hypothesized to contribute to the inward force on spindle poles by shortening the MTs connecting the poles and chromosomes and by sliding inward ipMTs, respectively, and when either of these motors is inhibited, spindle length increases.

Recently, mathematical modeling (reviewed in Gardner and Odde, 2006; Mogilner *et al*, 2006) was used to examine the role of forces and MT dynamics in spindle development (Nédélec, 2002; Cytrynbaum *et al*, 2003; Brust-Mascher *et al*, 2004; Gardner *et al*, 2005; Civelekoglu-Scholey *et al*, 2006; Burbank *et al*, 2007; Cheerambathur *et al*, 2007). For example, one of these models explained pre-nuclear envelop breakdown spindle elongation to the steady state during prophase as being the result of a balance between a constant cortical dynein-generated force pulling asMTs outward and an antagonistic spindle length-dependent Ncd-generated force pulling the ipMTs that link the poles inward (Cytrynbaum *et al*, 2003). Another model (Brust-Mascher *et al*, 2004) quantitatively explained how the persistent sliding apart of ipMTs by kinesin-5 motors, combined with changes in the activity of an antagonistic MT depolymerase on the spindle poles, produces poleward flux in pre-anaphase B spindles and drives anaphase B spindle elongation. These models provided a successful description of the experimental data because of the relative biochemical simplicity of prophase, during which most mitotic motors are sequestered in the nucleus and do not contribute to the pole–pole separation mechanism, and the structural simplicity of anaphase B, during which the ipMTs dominate spindle pole dynamics. However, even these relatively simple models were based on guessing (plausible values of) a formidable number of parameters. When model complexity grows beyond certain level, intuition alone is insufficient. Reverse engineering, an approach complementary to this 'explicit' modeling of a simplified system, uses computational optimization to automatically identify the appropriate model parameter values by constraining the parameters with quantitative experimental data.

Now that the inventory of mitotic force-generating and regulatory molecules is close to completion (e.g. Bettencourt-Dias *et al*, 2004; Goshima *et al*, 2007), the task of elucidating the mechanism of action of the mitotic spindle at a systems biology level is becoming realistic. Part of this task is to 'reverse engineer' the spindle—i.e. using experimental data to understand the temporal activation sequence and the mechanical characteristics of the force generators acting during mitosis—and reconstituting the spindle *in silico*. This presents a challenge that seems prohibitive: with more than 10 molecular motors being involved, each characterized by unknown mechanical, kinetic and regulatory parameters, and the structural complexity of the spindle, especially in metaphase, it is impossible to use intuition and traditional modeling to explain the dynamics associated with the sequence of transitions characteristic of mitotic progression. To address this challenge, here we develop and utilize a novel computational algorithm that automatically builds force balance models from a few MT–motor modules and uses quantitative experimental data to screen and optimize them. This algorithm ultimately identifies all plausible activation sequences and mechanical characteristics of the molecular motors that mediate spindle elongation in the *Drosophila* embryo.

Results

Force balance model

We divide the complex spindle machinery into its elementary structural components based on four distinct MT populations that are known to act within the spindle, namely astral (asMT) inter-polar (ipMT), chromosomal (chrMT) and kinetochore (ktMT) (Figure 1B). For each MT population, we first calculate the force acting on a single MT. For example, to obtain the force acting on a single chrMT, we consider two possible scenarios shown in Figure 1B. In the first case, the chrMT's minus end is anchored at the pole, while its plus end is connected to the chromosome through the chromokinesin motor on the chromosome arm. Then, the relative velocity between the motor and the chrMT is the difference between the pole velocity, V_{pole}, and the chromosome velocity, V_{chr}. We characterize each mitotic motor with an assumed linear force–velocity relation (Nédélec, 2002; Cytrynbaum *et al*, 2003) characterized by two parameters—maximal stall force and free unloaded velocity (in this case, $F_{\mathrm{chr,mx}}$ and $V_{\mathrm{chr,mx}}$, respectively): if the MT does not move relative to the motor, then the motor pushes the MT in the poleward direction with the maximal, stall, force. However, if the MT slides poleward with the rate (V_{pole}–V_{chr}) relative to the chromokinesin motor, then the force exerted by this plus-end-moving motor on the chrMT is lower,

$$F_2 = F_{\mathrm{chr,mx}}\left(1 - \frac{V_{\mathrm{pole}} - V_{\mathrm{chr}}}{V_{\mathrm{chr,mx}}}\right) \qquad (1)$$

(there is zero force if $V_{\mathrm{pole}}-V_{\mathrm{chr}}=V_{\mathrm{chr,mx}}$). In principle, multiple force generators can contribute to this force on the chromosome arm, including MT polymerization. In the model, we combine them into one single 'composite' motor and assume that it can be characterized by a linear force–velocity relation.

An alternative possibility is that the chrMT is not anchored at its minus end, but rather is being actively depolymerized by the pole-associated MT depolymerase (i.e. kinesin-13, or a combined effect of all the MT depolymerases; Figure 1B). In this case, we have to consider the force balance on this MT. Since the viscous drag for a single MT is negligible (Howard, 2001), we simply have to balance two motor forces (on the chromosome arm and at the pole: left- and right-hand sides of

the equation, respectively), each characterized by its own force–velocity relation:

$$-F_{\mathrm{chr,mx}}\left(1-\frac{V^{\mathrm{chr}}_{\mathrm{speckle}}-V_{\mathrm{chr}}}{V_{\mathrm{chr,mx}}}\right)=F_{\mathrm{dep,mx}}\left(1-\frac{V^{\mathrm{chr}}_{\mathrm{speckle}}-V_{\mathrm{pole}}}{V_{\mathrm{dep,mx}}}\right) \quad (2)$$

where $V^{\mathrm{chr}}_{\mathrm{speckle}}$ is the velocity of the chrMT in the laboratory frame of reference (that could be observed as the velocity of a fluorescent tubulin 'speckle'). Linear equation (2) is easily solved, giving us the chrMT velocity $V^{\mathrm{chr}}_{\mathrm{speckle}}$ such that the motor forces acting on that MT are balanced. Then, the force pushing the spindle pole outward can be computed by substituting this $V^{\mathrm{chr}}_{\mathrm{speckle}}$ into the negative depolymerase force:

$$F_3=-F_{\mathrm{dep,mx}}\left(1-\frac{V^{\mathrm{chr}}_{\mathrm{speckle}}-V_{\mathrm{pole}}}{V_{\mathrm{dep,mx}}}\right) \quad (3)$$

To compute the total force on the chrMT population, we have to determine which motors are active and when. We do not explicitly model the mitotic regulatory network, but rather reduce it to the effective binary 'on' and 'off' 'switches' of the molecular motors. We define the binary switch time-dependent parameters $P_{\mathrm{dep}}(t)$ and $P_{\mathrm{chr}}(t)$ (for depolymerase and chromokinesin) that are equal to 1 if the respective motor is engaged and generating force and either MT movement or growth/shortening occurs and to 0 otherwise. Using these switch parameters and equations (1) and (3), we obtain the total force on the entire population of chrMTs:

$$F_{\mathrm{chr}}(t)=P_{\mathrm{chr}}(t)N_{\mathrm{chr}}\frac{A_{\mathrm{chr}}}{\pi(S-D)^2}\times\left(\left(1-P_{\mathrm{dep}}(t)\right)F_2+P_{\mathrm{dep}}(t)F_3\right) \quad (4)$$

Equation (4) works as follows. Expression $F=((1-P_{\mathrm{dep}}(t))F_2+P_{\mathrm{dep}}(t)F_3)$ represents the single MT force: if the depolymerase at the pole is active, $P_{\mathrm{dep}}=1$, and $F=F_3$, otherwise, $P_{\mathrm{dep}}=0$, and $F=F_2$. N_{chr} is the total number of chrMTs, so $N_{\mathrm{chr}}F$ is the maximal possible total chrMT force. If the chromokinesin motor is active, $P_{\mathrm{chr}}=1$, otherwise $P_{\mathrm{chr}}=0$ and the whole force is zero. Finally, A_{chr}, additional parameter, is the chromosome arm area, while the difference between $S(t)$, the pole-to-pole distance, and $D(t)$, the inter-sister chromatid distance, is the double pole-to-chromosome distance. The dimensionless geometric factor $A_{\mathrm{chr}}/\pi(S-D)^2$ determines the fraction of the MTs impinging on the chromosome arm.

Similar arguments are used in the Supplementary information to calculate the total forces F_{ip}, F_{aster} and F_{kt} acting on the three other MT populations, and we summate them to obtain the total forces applied to the spindle pole, $F_{\mathrm{ip}}+F_{\mathrm{chr}}+F_{\mathrm{aster}}-F_{\mathrm{kt}}$, and to the chromosome, $F_{\mathrm{kt}}-F_{\mathrm{chr}}-F_{\mathrm{cohesion}}$. (The results indicate that the kt forces are usually directed inward, while all others outward, hence the expression to the resulting net outward force on the pole. A chromosome is pulled outward by the kt force resisted by inward chromokinesin force and cohesion between the sister chromatids; the latter is approximated by a linear spring.) One additional twist of the model is that to calculate the ipMT forces, we calculate the dynamic overlap between the ipMTs at the spindle equator and assume that two active motors (kinesin-5 and -14) and passive crosslinkers generate additive sliding forces proportional to the overlap length. In the low Reynolds number environment of the cell, pole and chromosome separation velocities are determined by the balance of the total MT and cohesion forces and the effective viscous drag (Nédélec, 2002; Cytrynbaum *et al*, 2003; Brust-Mascher *et al*, 2004; Civelekoglu-Scholey *et al*, 2006):

$$\frac{\mu_{\mathrm{pole}}}{2}\frac{\mathrm{d}S}{\mathrm{d}t}=F_{\mathrm{ip}}+F_{\mathrm{chr}}+F_{\mathrm{aster}}-F_{\mathrm{kt}} \quad (5)$$

$$\frac{\mu_{\mathrm{chr}}}{2}\frac{\mathrm{d}D}{\mathrm{d}t}=F_{\mathrm{kt}}-F_{\mathrm{chr}}-F_{\mathrm{cohesion}} \quad (6)$$

where μ_{pole} and μ_{chr} are the effective pole and chromosome drag coefficients, respectively. (The coefficients $\frac{1}{2}$ are included to account for the fact that the pole and chromosome rates of movement away from the spindle equator are half that of the respective pole–pole and chromosome–chromosome separation velocities.) By solving equations (5) and (6), we recover the temporal dynamics of spindle poles and chromosomes.

Thus, our model has a modular character: we construct the 'virtual spindle' (Figure 1A) from the 'building blocks'—eight possible MT–motor configurations (Figure 1B)—using a combinatorial approach, in which the 'building blocks' composition changes over time based on the 11 time-dependent binary switch parameters representing the activity timing of all major known force generators in the spindle (Figure 1). We allow each motor to switch its activity only once during mitosis: the ith motor (where $i=1,\ldots,8$) is active or not active all the time, or it is active (inactive) in the beginning and switches off (on) at a random time t^i_{switch}. In addition to these 8 switching times, each such virtual spindle is characterized by a random choice of 3 more switching times (regulating changes in MT numbers and chromosome cohesion), 16 stall forces and free unloaded velocity of 8 mitotic motors, and 8 other geometric, kinetic and mechanical parameters, 39 parameters in total. Each parameter's value can vary in certain wide range justified by available information (see the Supplementary information, Supplementary Table 1). This formulation allows us to define a 39-dimensional 'model parameter space' and encode multiple models by points in this space corresponding to a large number of possible combinations of force–velocity relations, variations in the kinetics and timing of the regulatory switches.

The model is simple, based on drastic assumptions of perfectly symmetric, an effectively one-dimensional spindle, a homogenous distribution of motors, no dependence of motor affinity on the generated forces, only binary variations in the motor activities and MT numbers, additive multiple motor forces, etc. Even with this conceptual simplicity and a relatively small number of spindle structural elements, the total number of possible ways in which multiple mitotic motors of various characteristics can be integrated to build different mitotic spindles is astronomical. Thus, a straightforward scan of the entire model space is impossible, and we resort to the stochastic optimization process to identify the model parameters that obey experimental constraints.

Results of computational searches of the model space

To determine if the temporal regulation of mitotic motors' activity is essential, we searched for 'virtual spindles' that could mimic the spindle elongation in WT embryos (Figure 1C) without any motor switching during mitosis, and we did not identify any good fit for the data under these conditions. We then searched for models that could explain the kinetics of spindle pole separation (Figure 1C) and chromosome motility (Supplementary Figure 4) in WT embryos, with motors allowed switching on or off only once. The number of models identified this way was very high (~10 000). Figure 2A–D shows the time series for forces acting on four MT populations in the virtual spindle for just four out of the thousands of different models that agree with the WT data predicting almost exactly the time series for WT spindle elongation in Figure 1C. In the first two of these models (Figure 2A and B) that are very similar to each other, the spindle is governed by a large inward ktMT force being balanced by a large outward force generated by chrMTs. The ipMT and asMT forces in these two models are almost negligible. In the third, conceptually different, model (Figure 2C), all four MT populations participate in the force balance, but only up to the anaphase onset, after which all forces decrease by several orders of magnitude from hundreds to single picoNewton range. In the fourth, also very distinct, model (Figure 2D), the forces generated by all four MT populations are significant at certain time intervals (Supplementary information and Supplementary Figure 2).

To analyze the multiple models statistically, we developed a quantitative distance measure that estimates how similar pairs of models are. This distance measure is based on differences in the magnitudes of forces and in the activity profiles for model pairs (Supplementary information). To illustrate the inter-model distances that are hard to visualize in high (39-) dimensional parameter space, we used this distance measure and projection onto a two-dimensional manifold in the model parameter space (Supplementary information; Figure 2E). In this figure, the metric two-dimensional distance between the model pairs reflects the multi-dimensional distance between full parameter sets characterizing the pairs of models. The positions of four sample models from Figure 2A–D in this projection, the quantitative similarity of models A and B, and significant differences among models B–D can be seen in Figure 2E.

The results of this first search lead us to the following conclusions: (i) there is a tremendous variety of plausible model parameters that can explain the WT behavior, whose combination can be complex and counterintuitive—there is no way to come up with a motor combination generating the force sequence shown in Figure 2D, for example. So, the WT data set, on its own, is not sufficient to discriminate between the multiple potential mechanisms of mitosis in this system. (ii) Many models are qualitatively different from each other, like those illustrated in Figure 2B–D, but some are very similar to each other, such as the pair shown in Figure 2A and B—the difference between those is in the small variation of a few parameters, and biologically, this pair describes basically the same molecular mechanism. This demonstrates the need for proper clustering of the models resulting from the computer search.

Clustering analysis (Supplementary information and Supplementary Figure 3) of the ~10 000 models identified ~1000 distinct model groups. Even this large number of possible distinct model types is an underestimate of the expected number of force integration scenarios. Convergence analysis (Supplementary information) showed that the search is still far from a complete exploration of total model space, and we estimate that there are ~1500 possible model groups that can explain the WT data (Supplementary information).

To further constrain plausible models, we repeated the above search in an iterative manner, using at each iteration more of the experimental data on the dynamics of spindle length following inhibition of different motors (Figure 1C), in addition to the WT data. Specifically, we first used data for both WT spindles plus those with inhibited dynein, then WT, dynein- and kinesin-5-inhibited spindles, then we added data for kinesin-13-inhibited spindles, then for kinesin-14-null spindles and finally we incorporated the data for kinesin-5-inhibited/kinesin-14-null spindles (explained in Figure 1). The models were deemed successful if they predicted, with only a small error, the time series for spindle length dynamics both for WT, and for experimentally perturbed spindles. At the present, we do not have the data for the time-dependent inter-chromosomal distance for the perturbed spindles; as discussed in the Supplementary information, such data probably would not be of much use constraining plausible models. With each iteration, the search was conducted independently of previous iteration thereby not restricting the possible models to ones that were previously identified.

As expected, we saw that the addition of more experimental data decreased the number of identified model groups. Figure 2F shows the predicted number of groups from the convergence analysis as the experimental data accumulate. We saw that from ~1500 model groups, when only WT data were used, there were only 6 different model groups 'surviving' the scrutiny of the whole body of the experimental data after 5 iterations. Furthermore, with each additional iteration, the models that were in agreement with more experimental data occupied a lesser segment of the parameter space (shown in the two-dimensional projection (same as that in Figure 2E) in Figure 2G). This suggests that the additional experimental data can indeed constrain the number of viable spindle models. This trend can be seen further in the properties of individual components of the spindle machinery. For example, Figure 2H shows the probability density estimates of two parameters (switching time and force) that characterize the kinesin-14 motor, Ncd. The initially wide and almost unconstrained distributions of the possible parameter values obtained when only WT data are used are observed to narrow down significantly as the additional inhibition data are used. A similar trend was seen for parameters characterizing other force generators.

Comparison of conserved model features with experimental data

The final result of this iterative elimination process is a set of ~1000 models that are clustered into six groups (Figure 3; the temporal changes in total force generated by each MT array and the 'on–off' motor switching are shown for all

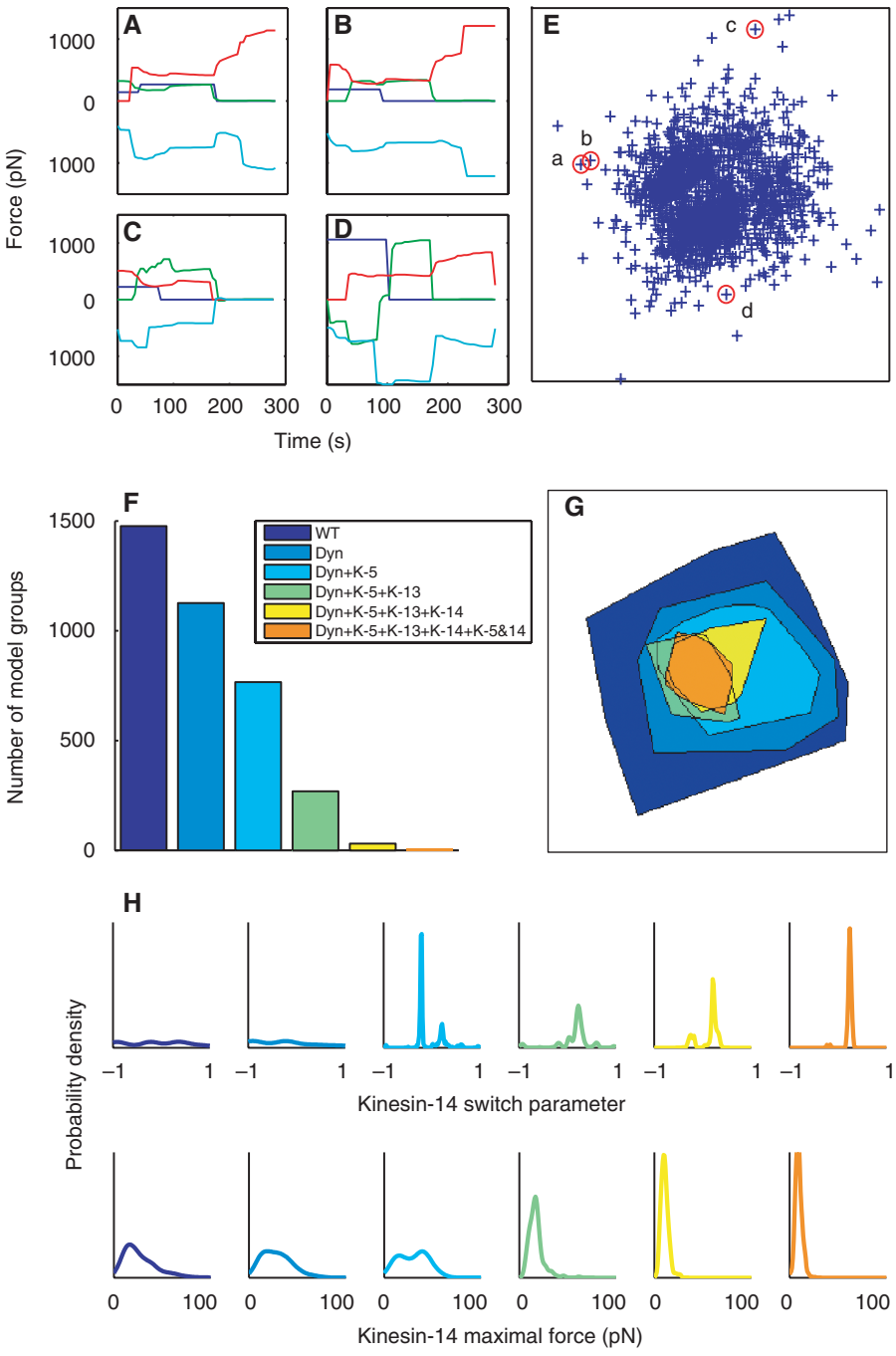

Figure 2 Iterative elimination of models that do not fit experimental data. Initial analysis identified ~10 000 models (belonging to ~1500 groups) that agree with WT data. (**A**–**D**) Four examples of the forces on the four MT populations (asMT—blue; ipMT—green; chrMT—red and ktMT—cyan) in different models. (**E**) Crosses illustrate projections of the points in the parameter space corresponding to all identified models onto a two-dimensional manifold in the parameter space (explained in the Supplementary information). The models corresponding to (A–D) are marked with red circles. The iterative process of addition of experimental data to the search reduced the number of identified groups of models (**F**) and the area they occupy in the two-dimensional projection of model space (**G**) (same projection as that in (E)). The probability density distributions of the parameter values governing the timing of kinesin-14 activity and force for each iteration are shown in (**H**) with the same color coding as that in (F).

these models in Figure 3A and for one selected model as an illustrative example in Figure 3B). Convergence analysis suggests that the search reached saturation and that all possible model types were identified (Supplementary information and Supplementary Figure 2). Interestingly, though the available data are insufficient to definitively narrow down the number of spindle model groups to one, thereby identifying the ultimate *Drosophila* spindle model, we discovered that several model properties were highly conserved among all ~1000 models belonging to the six final groups, hinting that these properties are required for proper spindle design and mitotic progression in this system.

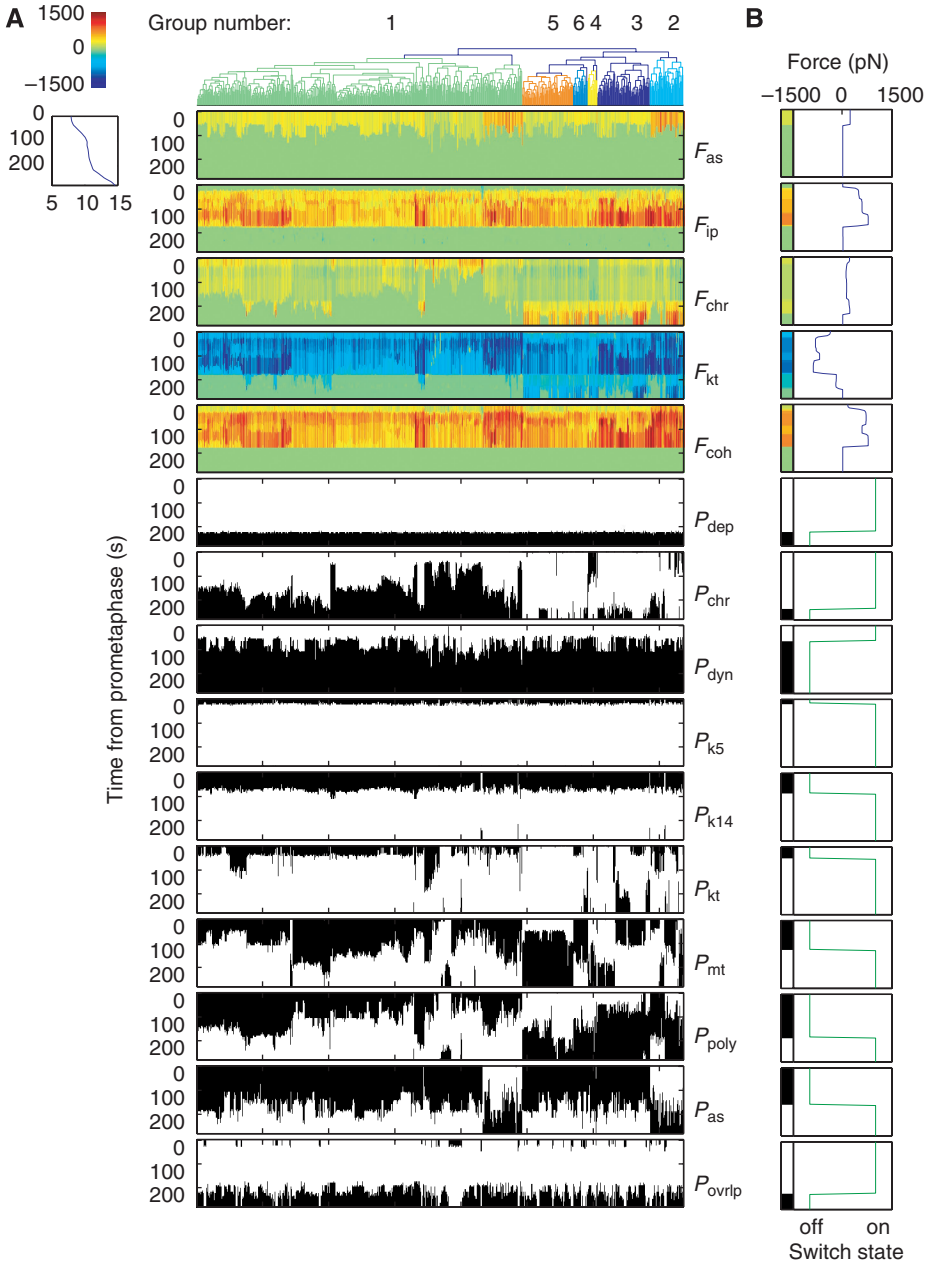

Figure 3 Cluster analysis of all identified models. (**A**) Results of the cluster analysis for models that fit all available experimental data. Dendrogram shows the hierarchical tree of all ~1000 models. Each imaginary vertical line across the panel corresponds to a specific model fitting all available experimental data. Time series (represented on the *y* axis of each panel running from top (early) to bottom (late)) for the forces on the four MT populations and cohesion forces from prometaphase (t=0) till the end of anaphase B (t=278 s) follow immediately below the dendrogram. Six identified clusters within the tree are color-coded. The forces (in picoNewtons) are color coded according to the bar shown at the upper left corner (extreme red (blue) corresponds to 1500 pN (−1500 pN)). The forces are abbreviated as follows: F_{as}—total force on astral MTs; F_{ip}—total force on inter-polar MTs; F_{chr}—total force on MTs reaching to the chromosome arms; F_{kt}—total force on the kinetochore fiber and F_{coh}—forces induced by the cohesion complex that hold sister chromatids together. For the reference, the time series for the pole–pole distance are shown immediately below the force bar. Time series for 10 motor switches' activity follow immediately below the force time series. White and black correspond to active and inactive motors, respectively. The switches are: P_{dep}—pole depolymerizer; P_{chr}—chromokinesin; P_{dyn}—dynein; P_{k5}—kinesin-5 sliding motor; P_{k14}—kinesin-14; P_{kt}—combined kt motors; P_{mt}—MT plus end depolymerization activity at the kinetochore; P_{poly}—MT plus end polymerization activity at the kinetochore; P_{as}—switch regulating the number of astral MTs; P_{ovrlp}—switch regulating the number of MTs at the overlap zone at the spindle equator. (**B**) The time series for the forces and switches predicted by a single selected model from group 1 as an illustrative example. The vertical bars (left) in the upper half of the panel represent the color-coded forces for each MT population, whereas the corresponding graphs (blue line, right) depict the change in magnitude of the corresponding force with time. The vertical bars in the lower half of the panel (left) represent the black–white switching 'off' or 'on' of the specific motors at the times indicated on the graphs (green line, right) for this particular model.

Thus, in all the models, the depolymerase(s) (P_{dep} in Figure 3), shortening the MTs at the pole thereby counteracting the outward thrust of other motors, must be active throughout mitosis to restrain spindle elongation, and must be switched off only at the onset of anaphase B to allow rapid pole–pole separation, in agreement with previous experimental data

(Brust-Mascher and Scholey, 2002; Brust-Mascher *et al*, 2004; Rogers *et al*, 2004). The timing of kinesin-5 activity (P_{k5} in Figure 3) is also highly conserved among all the models. This motor has to be switched on during prometaphase to exert outward forces on ipMTs until the end of anaphase B and it is the main force generator sliding the poles apart, again in agreement with experimental observations (Sharp *et al*, 1999). Dynein (P_{dyn} in Figure 3) switches off uniformly before the end of metaphase and does not contribute to the outward force in the end of mitosis—this model prediction is surprising, since previous work suggested that cortical dynein contributes to spindle pole separation during late anaphase B (Sharp *et al*, 2000b). This (possibly transient) downregulation of dynein activity would be hard to predict using intuition without the system-level search, and it needs to be tested in the future.

Also, the forces exerted on asMTs and ipMTs are conserved: outward asMT forces of hundreds of picoNewtons pull the poles apart before metaphase and switch off afterward, and then ipMT sliding forces of hundreds of picoNewtons take over and push the poles apart during late prometaphase and metaphase and drastically decrease at the anaphase onset. All six model groups predict that the spindle is largely balanced by the outward ipMT forces, assisted at early stage by asMT forces and by inward ktMT forces. The magnitude of the forces and the timing of their action are model predictions that can be tested in the future. Other conserved mechanical features are discussed in the Supplementary information.

In addition to illuminating properties of the entire spindle, the modeling suggests that specific biophysical properties of the participating molecular motors are conserved. The plus-end-directed kinesin-5 and minus-end-directed kinesin-14 motors are proposed to act antagonistically on the antiparallel overlap zone of the ipMTs (Figure 1). Our search predicts that to reproduce the experimental results, kinesin-5 should be strong (great stall force) and slow (small unloaded velocity), while kinesin-14 should be weak (small stall force) and fast (great unloaded velocity). Figure 4 shows the predicted force–velocity curves for these two motors. Interestingly, this prediction was recently supported by *in vitro* biochemical studies: the experimentally measured unloaded velocities of the two motors are shown in the inset of Figure 4; indirect measurements reported in Tao *et al* (2006) are consistent with the notion that the stall force of kinesin-5 is greater than that of kinesin-14. Note, that the predicted motors' force–velocity relations (Figure 4) illustrate the robustness of the models to a few-fold parameter fluctuations, but not to order of magnitude changes. Qualitative feature of intersection of the force–velocity curves of the opposing motors is conserved as well. Predictions of other motors' force–velocity properties can be gleaned from the Supplementary information, Supplementary Table 3 and Supplementary Figure 6.

Open questions: differences between the six identified model groups

While many of the model features are conserved among all identified models, the six identified model groups have interesting biological differences among them summarized in Table I. Group 1 is unique in its difference from the other five

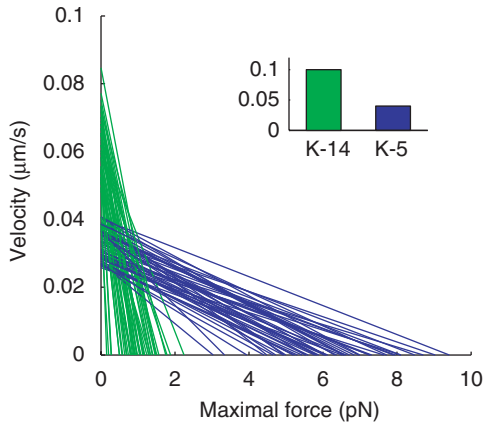

Figure 4 Constraints on the motors' mechanical properties. The predicted force–velocity relations of kinesin-5 (blue) and kinesin-14 (green). The main panel shows the force–velocity relation predicted in 50 resulting models randomly chosen from ~1000 models that fit all available experimental data. The inset shows free load velocity measurements reported in Tao *et al* (2006).

Table I Differences among six identified model groups

Group number	1	2	3	4	5	6
Strong cortical forces during prometaphase	–	+	–	–	–	–
Chromosome arm forces—active during prometaphase	+	+	+	–	+	+
Chromosome arm forces—active during anaphase B	–	+	+	+	+	+
ktMTs are in polymerization state during prometaphase	–	–	–	+	+	–
ktMTs are in depolymerization state during metaphase	–	–	+	–	–	–
ktMTs are in polymerization state during anaphase B	+	–	–	–	–	–

groups in the following respect: outward forces resulting from chromosome arms, due either to chromokinesins or to MT polymerization, are downregulated during anaphase B. To maintain the balance of forces, the inward kt forces in this group are much smaller in magnitude than in the rest of the groups. This smallness is due to ktMT polymerization counteracting the effect of the inward-thrusting motors. Therefore, in this group of models, the balance of small, picoNewton-level forces is characteristic for the anaphase B spindle, unlike hundreds of picoNewton forces at the end of mitosis predicted by all other groups. The largeness of the parameter space corresponding to this group (Figure 3) could also mean that this is the most robust strategy of the spindle design, though at the present we cannot support or reject this statement. Below, we describe in detail the sequence of molecular events predicted by this group.

Group 2 is unique among the six groups since it is the only one that has a strong component of cortical forces that contribute to prometaphase elongation. Mechanistically, this is achieved by having a high number of asMT (~200) with the cortical dynein active and pulling on the asMTs comparing to a low number of asMT (~20) in the rest of the groups. Although in groups 2–6, forces on the chromosome arms are generated during anaphase B, in groups 2–3 and 5–6, these forces'

contribution starts early in prometaphase, whereas group 4 is unique in that the chromosome arm forces are activated only during anaphase B. The rest of the differences among the remaining groups all result from differences in ktMT dynamics. Group 3 is unique since it is the only group where ktMT switch into depolymerization mode in metaphase. Groups 4 and 5 have ktMTs in polymerization state in early prometaphase, while in group 6, ktMTs are inactive until they start depolymerizing during anaphase B. Mechanistically, these differences in ktMT activity are achieved by differences in the switching times regulating activities of several participating motors and MT dynamics.

Predicted sequence of molecular events guiding spindle elongation

We chose one of the models from the largest model group 1 to describe the predicted sequence of molecular events guiding the spindle elongation (Figure 5). In this model, at the beginning of prometaphase, cortical dynein pulling forces supported by pushing forces from the chromosome arms are balanced by inward forces resulting from MT minus end depolymerization at the poles. Then, recruitment of kinesin-5 to the antiparallel ipMTs increases the net outward force, while dynein is switched off followed by the switching on of MT depolymerases at the kts. All these pre-metaphase events result in relatively small force balance changes, because strong antagonism between kinesin-5 and kinesin-13 on ipMTs largely determines the total force. Upregulation of kinesin-14 then reduces the net ipMT outward force to produce the metaphase steady state and the subsequent downregulation of the chromosome arm forces and degradation of cohesins substantially reduce the ktMT tension and mark the transition to anaphase A. Finally, anaphase B is the result of the switching off of MT depolymerization at the poles. Figure 5A shows the predicted time series for the spindle length, faithfully imitating the WT data. Figure 5B shows the forces acting on all four MT populations and generating the predicted spindle elongation, while Figure 5C illustrates the timing of switching of the mitotic motors responsible for generation of these forces. Prediction of this, likely most plausible, mechanistic scenario of the *Drosophila* embryo mitotic spindle elongation is arguably the most valuable modeling result, and would have been impossible to obtain without such a massive computer search.

Testable predictions generated by modeling

Variability of the multiple resulting mechanisms suggests that a few alternative activity profiles of mitotic force generators

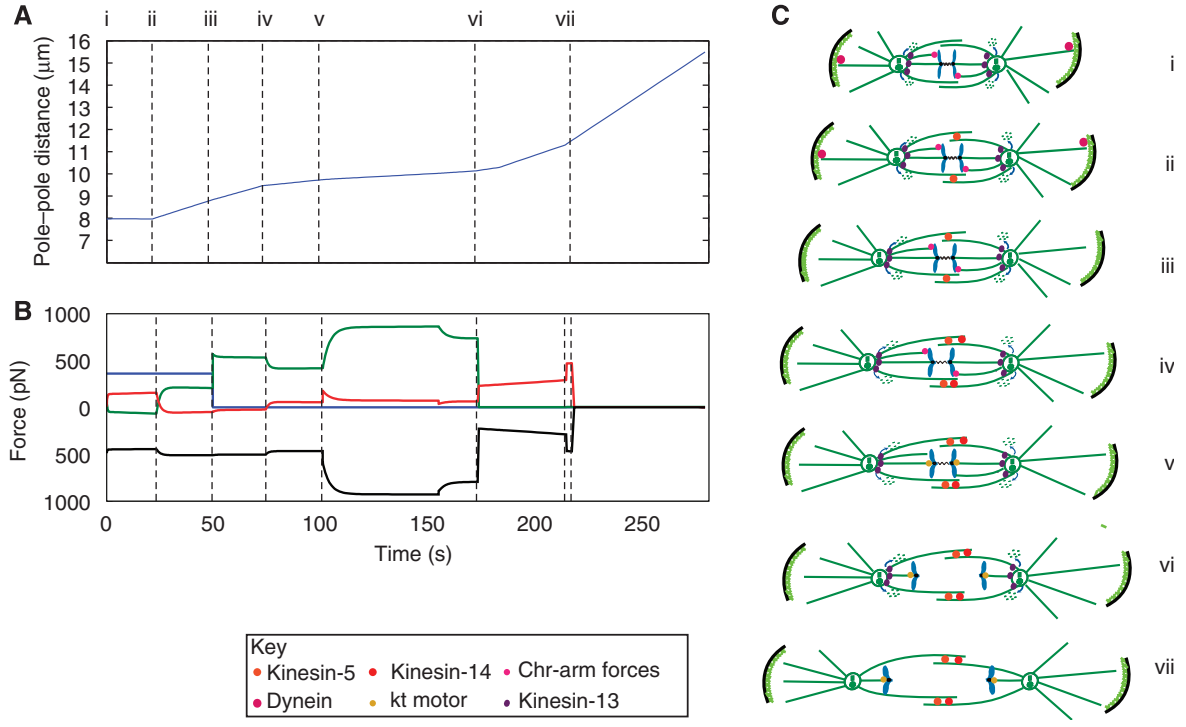

Figure 5 Example of an identified model. The identified forces and main switches in one of the identified models (from group 1). (**A**) The pole–pole distance resulting from the net force acting on the spindle poles. (**B**) The MT populations' forces: asMT (blue), chrMT (red), ipMT (green) and ktMT (black). (**C**) The predicted sets of force generators acting in the spindle at sequential mitotic stages; roman numerals correspond to the stages in (A, B). (i) At the beginning of prometaphase, dynein pulling forces supported by pushing forces from the chromosome arms are balanced by inward forces resulting from MT minus end depolymerization at the poles. (ii) Recruitment of kinesin-5 to the antiparallel ipMT tips increases the net outward force. Then, downregulation of dynein (iii) followed by upregulation of kinesin-14 (iv) antagonizes kinesin-5, reduces the ipMT outward force (B) and decreases the total outward force resulting in the metaphase steady state. Upregulation of kt motors (v) changes the composition of the balance of forces (B) but has very small net effect on the total force (A). These changes followed by the degradation of cohesion (vi) are the only necessary transitions required for progression through anaphase A. Finally, anaphase B is the result of downregulation of chr-arm forces immediately followed by downregulation of depolymerization at the poles (vii).

are possible and that further experimental work is needed to narrow down the number of groups and to identify the ultimate mechanism of spindle pole separation in *Drosophila* embryo mitosis. In other systems, it has been shown that chromokinesins are degraded in an APC-dependent manner during the metaphase-to-anaphase transition (Funabiki and Murray, 2000) and that this degradation is essential for entry into anaphase. It is yet to be determined whether this is the case in the *Drosophila* embryo system. The possibility that forces are generated by chrMT polymerization even after the chromokinesins are degraded further complicates the issue, so biophysical measurements of forces on the chromosome arms, as well as a chromokinesin-GFP-tagging experiment will be required to discriminate among models in group 1, group 4 and all other groups.

Time lapse movies of spindles with GFP-labeled tubulin (our unpublished data) together with immunofluorescence microscopy (Sharp *et al*, 1999) suggest that the density of asMT is higher during later stages of mitosis than in early stages. This evidence does not support group 2 where the number of asMT in prometaphase is predicted to be much higher than in the later stages. The caveat of this observation is that it is impossible to determine the exact number of asMTs that are actively engaged with the actin cortex by using GFP-tubulin studies alone. Reconstruction of the MT array using serial section electron microscopy (EM) at different stages of mitosis would be required to resolve this issue. Finally, determining the state of ktMTs is very challenging since it is very difficult to distinguish between the different MT populations, let alone their dynamic state, by using fluorescence microscopy. The use of EM could be very helpful in this respect as well: it will be possible soon to determine the MT dynamic state in a fixed EM image based on the MT structure. Systematic characterization of kt fibers during consecutive mitotic stages would provide information necessary to distinguish among groups 1, 3, 2–6, and 4–5. In principle, if and when the data described in these two paragraphs become available, Table I demonstrates that such data will be sufficient to choose a single model group from the current six possibilities.

The computational modeling described above also allows computer experiments, suggesting additional future experimental studies. Previous studies revealed that the double inhibition of both kinesin-5 and kinesin-14 fully rescues metaphase spindle assembly (Figure 1C, dashed blue line) (Sharp *et al*, 2000b), but in recent studies we observed that the inhibition of kinesin-5 in null mutants totally lacking kinesin-14 function sometimes caused a collapse of the spindle (Figure 1C, green line). While this apparent discrepancy requires further experimental scrutiny, its analysis using the model suggested that the observed differences in the extent of inhibition of kinesin-5 activity could be a critical factor. Specifically, we ran simulations of the models from group 1 that were modified so that the kinesin-5 motor was partially inhibited—its maximal force was factored by a parameter less than unity. The simulations predicted that the partial inhibition of kinesin-5 to a concentration of ~90% would result in a phenotype similar to that seen in embryos containing a WT level of kinesin-5. Further simulations predicted that the effect of more severe partial inhibitions of kinesin-5 would produce shorter metaphase spindle than those seen in WT spindles but

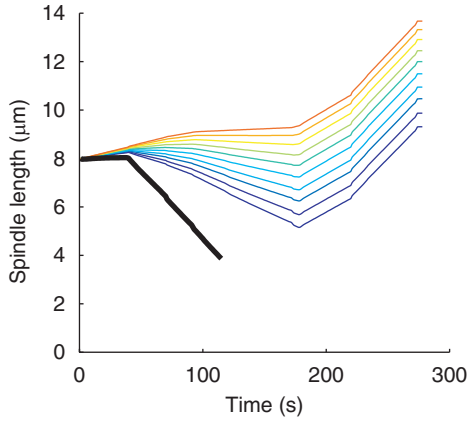

Figure 6 Model prediction. Simulation result of dynamics of spindle length over time after complete (black line) and partial (color lines) inhibitions of kinesin-5. Partial inhibition is from 80% (blue line) to 0% (red lines).

should have little effect on anaphase B spindle elongation (Figure 6). This prediction is in contrast with previous models for spindle length carried out in *Drosophila* S2 cells (Goshima *et al*, 2005), which suggested that metaphase spindle length is insensitive to the levels of kinesin-5. In addition, recent unpublished experiments suggest that the kinesin-5-dependent force balance that maintains the prometaphase spindle requires inward forces generated by kinesin-14 together with another unidentified factor. Our model further predicts that this additional inward force could be produced by a kinesin-13 depolymerase acting on ipMTs at the spindle poles and future experiments will be directed at testing this prediction. These examples illustrate the utility of our modeling strategy in identifying key, experimentally testable predictions.

Discussion

To summarize, we performed computer searches in the vast model space and identified six strategies for the temporal and structural organization of mitotic motors and MTs within the spindle, which quantitatively explain our observations of spindle elongation kinetics in WT, mutant and inhibited *Drosophila* embryos. Each of these strategies is characterized by specific activity timing and mechanical properties of each motor, MT number and a few other parameters. Note that the discovered models could not be obtained simply by combining earlier explicit models of specific mitotic stages, for example the inactivation of dynein (on asMTs) prior to the end of metaphase has not been considered nor suggested so far. Importantly, a number of features are conserved for all predicted models, including the timing of the activity of dynein and a few kinesins, as well as the forces and velocities of crucial mitotic motors. The search also revealed that large inward and outward forces in the range of hundreds of picoNewtons are closely balanced, which hints at a general design principle of mitotic spindle mechanics. In addition, the search also uncovered areas of uncertainties, mostly regarding the role of forces generated on the chromosome arms by MT polymerization and chromokinesins, the exact forces at the kts, and MT numbers and lengths. We make suggestions

about future experiments that could help to resolve these uncertainties.

The use of an unbiased systematic computational search revealed a plethora of models producing basically the same overall phenotype. Even the most restricted search identified hundreds of model variants, all predicting almost identical spindle dynamics. Polymorphism is well known to exist among protein molecules such as those composing parts of the mitotic machinery. Our analysis suggests that a parallel polymorphism exists in terms of accurate model representation, so that there is not necessarily 'one true model', but rather a set of models, all slightly different in their characteristics but capable of generating the same overall phenotype. This 'model polymorphism' makes our computational search approach a useful 'hypothesis generator' that can identify key experiments that are needed to further elucidate the mechanism of spindle elongation.

As is true for any model, our models depend on a set of assumptions, and this introduces a number of caveats into our modeling strategy. For example, (i) it is plausible that other, either known (e.g. kinesin-6), or yet to be identified, force generators act during mitotic progression; (ii) motor forces may not be additive; (iii) force–velocity relations may not be linear and (iv) motors may switch on and off more than once during mitosis. In addition, we assumed that the microinjected antibody inhibitors (Figure 1) serve only to reduce the effective concentrations of the target motor, but other effects (e.g. the antibody-induced inhibition of the mechanochemical cycle) could contribute to the observed inhibition (Ingold *et al*, 1988). Such problems will be addressed in future applications of our modeling methodology.

Furthermore, the large-scale search comes with a price. It requires using an approximation similar to a mean-field approximation in theoretical physics and other simplifying assumptions to reduce the computation time for each possible set of parameters. In reality, the *Drosophila* embryo spindle is highly stochastic (Cheerambathur *et al*, 2007), but this feature was ignored in the search. Incorporating realistic stochasticity, originating from MT dynamic instability and relatively small (in a thermodynamic sense) number of motors, into the entire search is computationally prohibitive, so instead we focused on investigating how the 'winning models' behave following incorporation of simplified stochasticity, such as white Gaussian noise and spread of individual MT lengths as a result of dynamic instability. The simulation results (not shown) demonstrated that incorporating the MT dynamic instability and additional stochasticity in motor concentration would not change the predicted pole–pole separation profile, supporting the deterministic approximation used in the large-scale search.

This study builds on and extends several previous spindle models that were developed for the *Drosophila* embryo (Brust-Mascher *et al*, 2004; Cheerambathur *et al*, 2007) and other systems (Nédélec, 2002; Burbank *et al*, 2007). We extended the idea of model screening and parameter search first proposed for spindle models by Nédélec (2002) and improved it from random sampling to more efficient search that uses repeated stochastic optimization. The improved efficiency is crucial since, unlike in the work of Nédélec (2002), in which the goal was to identify regions of parameter space that produce qualitatively interesting behavior, in this study the goal was to produce good fit to experimental data, similar to Gardner *et al* (2005).

Some predictions derived from all six groups of models appear to contradict available data (Sharp *et al*, 2000b; Brust-Mascher and Scholey, 2002). For example, the models predict that kinesin-14 is only activated after prometaphase, that ktMT flux is virtually absent during metaphase (Supplementary Figure 5) and that the partial inhibition of kinesin-5 produces instability in the metaphase steady states. These discrepancies indicate areas of uncertainty that merit further attention. It is possible, based on preliminary estimates, that changing assumptions (i) and/or (iii) would lead to a correct prediction of the timing of kinesin-14 activation, while changing assumption (iv) would lead to a correct value for ktMT flux. (In the present form, the model has ktMTs permanently attached to the kts and, in fact, agrees with recent observations of DeLuca *et al* (2006)). We see these inconsistencies as supporting the credibility and usefulness of the modeling, since they identify topics where further work is needed to reconcile theory and experiment, which is healthy for the discovery process.

The ultimate goal of systems biology is to construct comprehensive quantitative models for cellular function. One possible strategy is to 'build with a scaffold' (Ideker and Lauffenburger, 2003) by initially constructing coarse grain models and later building on the results of these models to construct more elaborate detailed models. The construction of the initial models can be based on high-throughput data or, as in our case, reverse engineering of simplified models. A few pioneering studies have used similar reverse engineering approaches to different biological systems (reviewed in Ma'ayan *et al* (2005)), mainly applying them to cell regulatory networks (Sachs *et al*, 2005). Our study applied a reverse engineering approach that uses global indirect quantitative data to perform a comprehensive computational search to identify the mechanical design of the spindle that can explain such data. Our strategy allows us to examine numerous possible parameter values and alternative mechanisms using coarse grain models and later refine the 'promising' models to include additional components with more detailed models. The suggested framework can be easily adapted to mitotic spindles in other organisms and *in vitro* (that may be designed differently) and, in fact, to many other biomechanical systems for which sufficient quantitative data exist.

Materials and methods

In brief, the analysis, performed automatically by the computer algorithm, proceeds as follows: (i) model parameters are chosen randomly from the allowed ranges; (ii) at each computational step, total MT forces for the four MT populations are found using equations similar to equation (4), the spindle geometry is updated by numerically solving equations (5) and (6), then the forces are updated for the updated geometry, etc., for the time $t \approx 280$ s. The solutions for each such parameter choice predict time series for the spindle forces and length. (iii) We collected several experimental data sets for time-dependent changes in spindle length in WT and experimentally perturbed spindles, and we averaged, smoothed and aligned the data (Supplementary information and Supplementary Figure 1; Figure 1C). The predicted time series for the spindle length are automatically compared with the corresponding data (Figure 1C), and a 'score' is

assigned to the model, so that if certain mathematical difference between the predicted and measured length time series is great, then the model's score is poor; while if the difference is small, the score is good (quantitative details in Supplementary information). The model is 'screened' so that if the score is poor (good), the model is discarded (selected). (iv) Another set of model parameters is chosen randomly, until thousands of 'good' models are amassed. (v) A genetic algorithm then automatically modifies or 'mutates' the successful 'selected' models, and repeated stochastic optimization results in the evolution of increasingly adequate multiple models, each producing excellent fits to all the available experimental data. (vi) Finally, a cluster analysis determines which of the adequate models are qualitatively different from each other, and which differ just by slightly distinct parameter values, and identifies minimal sets of successful strategies for force integration in mitosis. We conducted this optimization search process until a convergence analysis showed that the search had reached saturation and all possible model groups had been found. All optimizations and simulations were performed on an 11-node Linux cluster (each node had a 2× Opteron-246 processor) using a combination of Matlab and C codes. Full description of the details of the numerical analysis and computational search is provided in the Supplementary information.

Supplementary information

Supplementary information is available at the *Molecular Systems Biology* website (www.nature.com/msb).

Acknowledgements

We thank K Pollard for fruitful discussions. This study was funded by the University of California grant (UCBREP GREAT 2006-03) to RW, and by National Institutes of Health grants GM 55507 to JMS, GM068952 to AM and GM 068952 to AM and JMS.

References

Bettencourt-Dias M, Giet R, Sinka R, Mazumdar A, Lock WG, Balloux F, Zafiropoulos PJ, Yamaguchi S, Winter S, Carthew RW, Cooper M, Jones D, Frenz L, Glover DM (2004) Genome-wide survey of protein kinases required for cell cycle progression. *Nature* **432:** 980–987

Brust-Mascher I, Civelekoglu-Scholey G, Kwon M, Mogilner A, Scholey JM (2004) Model for anaphase B: role of three mitotic motors in a switch from poleward flux to spindle elongation. *Proc Natl Acad Sci USA* **101:** 15938–15943

Brust-Mascher I, Scholey JM (2002) Microtubule flux and sliding in mitotic spindles of *Drosophila* embryos. *Mol Biol Cell* **13:** 3967–3975

Brust-Mascher I, Scholey JM (2007) Mitotic spindle dynamics in *Drosophila*. *Int Rev Cytol* **259:** 139–172

Burbank KS, Mitchison TJ, Fisher DS (2007) Slide-and-cluster models for spindle assembly. *Curr Biol* **17:** 1373–1383

Cheerambathur DK, Civelekoglu-Scholey G, Brust-Mascher I, Sommi P, Mogilner A, Scholey JM (2007) Quantitative analysis of an anaphase B switch: predicted role for a microtubule catastrophe gradient. *J Cell Biol* **177:** 995–1004

Civelekoglu-Scholey G, Sharp DJ, Mogilner A, Scholey JM (2006) Model of chromosome motility in *Drosophila* embryos: adaptation of a general mechanism for rapid mitosis. *Biophys J* **90:** 3966–3982

Cole DG, Saxton WM, Sheehan KB, Scholey JM (1994) A 'slow' homotetrameric kinesin-related motor protein purified from *Drosophila* embryos. *J Biol Chem* **269:** 22913–22916

Cytrynbaum EN, Scholey JM, Mogilner A (2003) A force balance model of early spindle pole separation in *Drosophila* embryos. *Biophys J* **84:** 757–769

DeLuca JG, Gall WE, Ciferri C, Cimini D, Musacchio A, Salmon ED (2006) Kinetochore microtubule dynamics and attachment stability are regulated by Hec1. *Cell* **127:** 969–982

Funabiki H, Murray AW (2000) The *Xenopus* chromokinesin Xkid is essential for metaphase chromosome alignment and must be degraded to allow anaphase chromosome movement. *Cell* **102:** 411–424

Furuta K, Toyoshima YY (2008) Minus-end-directed motor Ncd exhibits processive movement that is enhanced by microtubule bundling in vitro. *Curr Biol* **18:** 152–157

Gardner MK, Odde DJ (2006) Modeling of chromosome motility during mitosis. *Curr Opin Cell Biol* **18:** 639–647

Gardner MK, Pearson CG, Sprague BL, Zarzar TR, Bloom K, Salmon ED, Odde DJ (2005) Tension-dependent regulation of microtubule dynamics at kinetochores can explain metaphase congression in yeast. *Mol Biol Cell* **16:** 3764–3775

Goshima G, Wollman R, Goodwin SS, Zhang N, Scholey JM, Vale RD, Stuurman N (2007) Genes required for mitotic spindle assembly in *Drosophila* S2 cells. *Science* **316:** 417–421

Goshima G, Wollman R, Stuurman N, Scholey JM, Vale RD (2005) Length control of the metaphase spindle. *Curr Biol* **15:** 1979–1988

Howard J (2001) *Mechanics of Motor Proteins and the Cytoskeleton*. Sunderland, MA: Sinauer Associates

Hoyt MA, Geiser JR (1996) Genetic analysis of the mitotic spindle. *Annu Rev Genet* **30:** 7–33

Ideker T, Lauffenburger D (2003) Building with a scaffold: emerging strategies for high- to low-level cellular modeling. *Trends Biotechnol* **21:** 255–262

Ingold AL, Cohn SA, Scholey JM (1988) Inhibition of kinesin-driven microtubule motility by monoclonal antibodies to kinesin heavy chains. *J Cell Biol* **107:** 2657–2667

Kapitein LC, Peterman EJ, Kwok BH, Kim JH, Kapoor TM, Schmidt CF (2005) The bipolar mitotic kinesin Eg5 moves on both microtubules that it crosslinks. *Nature* **435:** 114–118

Karsenti E, Vernos I (2001) The mitotic spindle: a self-made machine. *Science* **294:** 543–547

Kashina AS, Baskin RJ, Cole DG, Wedaman KP, Saxton WM, Scholey JM (1996) A bipolar kinesin. *Nature* **378:** 270–272

Kline-Smith SL, Walczak CE (2004) Mitotic spindle assembly and chromosome segregation: refocusing on microtubule dynamics. *Mol Cell* **15:** 317–327

Lawrence CJ, Dawe RK, Christie KR, Cleveland DW, Dawson SC, Endow SA, Goldstein LS, Goodson HV, Hirokawa N, Howard J, Malmberg RL, McIntosh JR, Miki H, Mitchison TJ, Okada Y, Reddy AS, Saxton WM, Schliwa M, Scholey JM, Vale RD (2004) A standardized kinesin nomenclature. *J Cell Biol* **167:** 19–22

Leslie RJ, Pickett-Heaps JD (1983) Ultraviolet microbeam irradiations of mitotic diatoms: investigation of spindle elongation. *J Cell Biol* **96:** 548–561

Ma'ayan A, Blitzer RD, Iyengar R (2005) Toward predictive models of mammalian cells. *Annu Rev Biophys Biomol Struct* **34:** 319–349

McDonald HB, Stewart RJ, Goldstein LS (1990) The kinesin-like Ncd protein of *Drosophila* is a minus end-directed microtubule motor. *Cell* **63:** 1159–1165

Mitchison TJ, Maddox P, Gaetz J, Groen A, Shirasu M, Desai A, Salmon ED, Kapoor TM (2005) Roles of polymerization dynamics, opposed motors, and a tensile element in governing the length of *Xenopus* extract meiotic spindles. *Mol Biol Cell* **16:** 3064–3076

Mitchison TJ, Salmon ED (2001) Mitosis: a history of division. *Nat Cell Biol* **3:** E17–E21

Mogilner A, Wollman R, Civelekoglu-Scholey G, Scholey JM (2006) Modeling mitosis. *Trends Cell Biol* **16:** 88–96

Nédélec F (2002) Computer simulations reveal motor properties generating stable antiparallel microtubule interactions. *J Cell Biol* **158:** 1005–1015

O'Farrell PH (2001) Triggering the all-or-nothing switch into mitosis. *Trends Cell Biol* **11:** 512–519

Oladipo A, Cowan A, Rodionov V (2007) Microtubule motor Ncd induces sliding of microtubules *in vivo*. *Mol Biol Cell* **18:** 3601–3606

Ostergren G (1951) The mechanism of co-orientation in bivalents and multivalents—the theory of orientation by pulling. *Hereditas* **37:** 85–156

Parry DH, O'Farrell PH (2001) The schedule of destruction of three mitotic cyclins can dictate the timing of events during exit from mitosis. *Curr Biol* **11:** 671–683

Peters JM (2002) The anaphase-promoting complex: proteolysis in mitosis and beyond. *Mol Cell* **9:** 931–943

Pines J, Rieder CL (2001) Re-staging mitosis: a contemporary view of mitotic progression. *Nat Cell Biol* **3:** E3–E6

Rogers GC, Rogers SL, Schwimmer TA, Ems-McClung SC, Walczak CE, Vale RD, Scholey JM, Sharp DJ (2004) Two mitotic kinesins cooperate to drive sister chromatid separation during anaphase. *Nature* **427:** 364–370

Sachs K, Perez O, Pe'er D, Lauffenburger DA, Nolan GP (2005) Causal protein-signaling networks derived from multiparameter single-cell data. *Science* **308:** 523–529

Saunders WS, Hoyt MA (1992) Kinesin-related proteins required for structural integrity of the mitotic spindle. *Cell* **70:** 451–458

Sawin KE, LeGuellec K, Philippe M, Mitchison TJ (1992) Mitotic spindle organization by a plus-end-directed microtubule motor. *Nature* **359:** 540–543

Scholey JM, Brust-Mascher I, Mogilner A (2003) Cell division. *Nature* **422:** 746–752

Sharp DJ, Brown HM, Kwon M, Rogers GC, Holland G, Scholey JM (2000b) Functional coordination of three mitotic motors in *Drosophila* embryos. *Mol Biol Cell* **11:** 241–253

Sharp DJ, McDonald KL, Brown HM, Matthies HJ, Walczak C, Vale RD, Mitchison TJ, Scholey JM (1999) The bipolar kinesin, KLP61F, cross-links microtubules within interpolar microtubule bundles of *Drosophila* embryonic mitotic spindles. *J Cell Biol* **144:** 125–138

Sharp DJ, Rogers GC, Scholey JM (2000a) Microtubule motors in mitosis. *Nature* **407:** 41–47

Tao L, Mogilner A, Civelekoglu-Scholey G, Wollman R, Evans J, Stahlberg H, Scholey JM (2006) A homotetrameric kinesin-5, KLP61F, bundles microtubules and antagonizes Ncd in motility assays. *Curr Biol* **16:** 2293–2302

Walker RA, Salmon ED, Endow SA (1990) The *Drosophila* claret segregation protein is a minus-end directed motor molecule. *Nature* **347:** 780–782

Supplementary Material - Table of contents

1. Description of 'model space'

1.1 Introduction

Here we derive a general model for spindle elongation during mitosis from prometaphase to the end of anaphase B. This derivation is based on calculating additive molecular motor forces that act on spindle poles and on ordinary differential equations describing the kinematics and movements of the spindle. To construct our model, we follow a reductionist approach and divide the spindle into its structural components – different populations of spindle microtubules (MTs) – and analyze each of the components separately. The analysis of each component is based on a detailed biophysical description of the balance of various MT/motor force generators. The spindle components are then combined together to form a complete 'virtual spindle'.

The spindle is highly dynamic and undergoes several transitions during mitosis. These transitions are a result of a complex biochemical regulatory network of kinases, phosphotases and proteolytic enzymes that regulate both force generators and spindle structure. To translate this regulatory network into mathematical language, we introduce the notion of binary switches. Binary switches are a simplified representation of the biochemical regulation during mitosis that controls the activity profiles of mitotic molecular motors, and, ultimately, mitotic forces. When certain switch is 'on' (=1), the corresponding motor is engaged and is 'force-generating'; when a switch is 'off' (=0), the motor is not engaged. We allow each force generator to switch at most once during mitosis, so respective variable P(t) is equal to either 0 or 1for the whole duration, or it switched from 0 to 1 at some $t = \tau$, or it switched from 1 to 0 at some $t = \tau$. τ is the random parameter, independently chosen for each switch. The different combinations of forces encoded by the switch parameters determine the overall time-dependent forces acting on the spindle poles and chromosomes. The model is general in the sense that tremendous number of possible multiple scenarios are encoded in the unified mathematical framework by the binary switch parameters and mechanical parameters for molecular motors. By 'shuffling' through all possible combinations of the multiple binary switches, and 'scanning' mechanical parameters, we can in principle generate every possible force balance model of the spindle.

To construct the model, we first divide the spindle MTs into four populations of different MT types: astral (asMT), inter-polar (ipMT), kinetochore (ktMT) and chromosome-arm (chrMT) (Fig 1b). In each of these MT populations, there are potentially several possible configurations of force generators on each single MT in that population. These configurations differ from each other based on the activity of different molecular motors that are localized on that MT population. Due to a negligible viscous drag and significant rigidity of each individual MT (Howard, 2001), MTs can be modeled as force propagators that connect either both poles (ipMT), or pole and chromosome (ktMT and chrMT), or pole and cell cortex (asMT). The analysis of each MT population starts with going through possible motor configurations on a single MT, and then combining single MTs mechanically to compute the total forces for each MT population. Finally, four MT populations are combined together with chromosome dynamics to calculate the overall spindle dynamics. The result is a set of differential-algebraic equations with time dependent parameters. These equations are solved numerically to generate the simulated pole and chromosome separation. Note, that our spindle has mirror symmetry: the spindle 'equator' does not move. The sister poles' speeds are equal in magnitude and opposite in direction, and so are sister chromatids' speeds. The velocities are positive

in the outward direction, so are the forces on asMTs, chrMTs, ipMTs (Fig 1b). The forces on ktMTs, however, are positive in the inward direction (Fig 1b). Note, that in Fig 5, the total ktMT force is plotted negative, opposing all other positive forces, for illustrative purposes.

We define the following model dependent variables (Fig 1a):

1. S – distance between the poles
2. D – distance between the sister chromatids
3. L – ipMTs' overlap length at the equator
4. V_{pole} - velocity of the pole.
5. V_{chr} - velocity of the chromosome.

To determine the above variables, we will derive a set of 5 differential equations to be solved numerically, dependent on the total forces on each MT population, also derived below. Note that $V_{pole} = \frac{1}{2}\frac{dS}{dt}$ and $V_{chr} = \frac{1}{2}\frac{dD}{dt}$.

1.2 Force on the asMT population

There is a unique possible single configuration of motors that can generate a force on asMT. In this configuration, Dynein is localized to the plus-end of the asMT and the asMT is anchored at its minus-end to the pole. This configuration is shown in Fig 1b. In section 1.2.1 we examine the force on a single MT and in section 1.2.2 we generalize to the whole population of asMTs.

1.2.1 Single MT analysis

When there is no depolymerizer at the minus-end, we assume that a MT is anchored to the pole either by the inactive depolymerizing motor or by some other anchoring protein. In the early developmental stage of *Drosophila* embryo, the distance from the pole to the cortex is constant (Cytrynbaum et al., 2005), so there are no relative pole/cortex movements, and no need to take into account Dynein's force-velocity relation. Therefore, the overall force will be constant and equal to the motor's maximal force:

$$F_1 = F_{dyn,mx}$$

1.2.2 Total force

Both the number of asMTs that reach the cortex and the number of active Dynein motors that generate force are important for the calculation of the total force. The number of asMTs can either increase or decrease. Here we approximate transitions between the two states by using a step function for the total number of asMTs. We assume two levels of the number of MTs reaching the cortex: low, N_{as}^{low}, and high, N_{as}^{high}. We define two switch variables that control the temporal behavior of the number of asMTs reaching the cortex and Dynein's activity as P_{as} and P_{dyn}, respectively. (They can be equal to 0 or 1, same as all other switches described below.) The total force generated by the asMT population is:

$$F_{as} = P_{dyn}\left(P_{as}N_{as}^{high} + \left(1-P_{as}\right)N_{as}^{low}\right)F_1 \quad (1)$$

If the Dynein switch parameter is equal to zero, Dyneins are inactive, and there is no pulling force on asMTs. If the asMT switch parameter is equal to zero, N_{as}^{low} asMTs pull the pole, otherwise N_{as}^{high} asMTs pull the pole. The switches described below regulate the total respective forces in a similar fashion.

1.3 Force on chrMT population

For chrMTs, there are two possible single chrMT configurations (Fig. 1b). In both configurations, the chrMTs are pushed away from the chromosome arms, either by plus-end polymerization or by chromokinesin motors. To simplify, we 'lumped' these two force generators into a single 'abstract' motor. What differentiates the two chrMT configurations is the activity of the minus-end depolymerizer. In 1.3.1 and 1.3.2, we analyze the two potential configurations, and in 1.3.3 we generalize to the entire MT population. Note, that we describe the motors mechanically with linear force-velocity relations (Brust-Mascher et al., 2004; Civelekoglu-Scholey et al., 2006) so that the effective motor-generated force is proportional to the relative velocity of this motor and the respective chrMT. The force is maximal at stall, when the relative velocity is zero. The force is equal to zero when the motor glides with its maximal velocity in the unloaded regime.

1.3.1 Without depolymerizer at the pole

Without depolymerization, we only need to consider one force-velocity relation:

$$F_2 = F_{chr,mx}\left(1-\frac{V_{pole}-V_{chr}}{V_{chr,mx}}\right) \quad (2)$$

where F_2 is the resulting force, $V_{pole}-V_{chr}$ is the motor velocity on the chromosome arm in the plus-end-direction relative to the pole, and $V_{chr,mx}$ is the unloaded gliding velocity of this motor. Below, similarly, more involved force-velocity relations are analyzed for other motors and configurations.

1.3.2 With depolymerizer at the pole

Here we need to consider the force balance between two motors – one at the minus-end, and another at the plus-end of the chrMT. Equalizing their generated velocity-dependent forces:

$$-F_{chr,mx}\left(1-\frac{V_{speckle}^{chr}-V_{chr}}{V_{chr,mx}}\right)=F_{dep,mx}\left(1-\frac{V_{speckle}^{chr}-V_{pole}}{V_{dep,mx}}\right)$$

we compute the velocity of a single chrMT ($V_{speckle}^{chr}$):

$$V_{speckle}^{chr}=\frac{\left(F_{dep,mx}\left(1+\frac{V_{pole}}{V_{dep,mx}}\right)+F_{chr,mx}\left(1+\frac{V_{chr}}{V_{chr,mx}}\right)\right)V_{dep,mx}V_{chr,mx}}{V_{dep,mx}F_{chr,mx}+V_{chr,mx}F_{dep,mx}} \quad (3)$$

Substituting this velocity into the previous equation, we find the total force on a single chrMT:

$$F_3=-F_{dep,mx}\left(1-\frac{V_{speckle}^{chrk}-V_{pole}}{V_{dep,mx}}\right) \quad (4)$$

1.3.3 Total force

The two configurations above assume that the chromosomal force generators are active. This is not necessarily the case. We therefore define a switch variable P_{chr} that controls the total force on this MT population. When $P_{chr} = 0$, the overall force on this MT population is zero. When $P_{chr} = 1$, the total force is a product of one of the two configurations' forces considered above by the total number of chrMTs that reach the chromosome. The choice of the configuration depends on the activity of pole depolymerization. Therefore, we define a switch parameter P_{dep} that controls this activity. When $P_{dep} = 0$, the force is F_2 and when $P_{dep} = 1$ the force is F_3. The total force is a product of the single chrMT force by the total number of chrMTs. The number of chrMTs reaching the chromosome arm is a function of the maximal number of MTs that are growing toward the chromosome $\left(N_{chr}\right)$, the surface area of the chromosomes $\left(A_{chr}\right)$, and the distance between the pole and the chromosome $\left(S - D\right)$. The mathematical representation of the above arguments is the following expression for the total force generated by the chrMT population:

$$F_{chr} = P_{chr} \frac{N_{chr} A_{chr}}{\pi \left(S - D\right)^2} \left(\left(1 - P_{dep}\right) F_2 + P_{dep} F_3 \right) \quad (5)$$

The denominator reflects the fact that the MT number reaching from the pole to the chromosome arm decreases with distance (Joglekar and Hunt, 2002).

1.4 Force on ktMT population

For ktMTs, there are three possible configurations (Fig. 1b), because force generators can be located on the minus-end, plus-end, or both ends of the single ktMT. In 1.1.6, 1.1.7 and 1.1.8, we analyze all three scenarios for a single ktMT and in 1.1.9 we generalize for the whole ktMT population.

1.4.1 Without depolymerizer at the pole

We consider three types of force generators at the kinetochore (kt). These represent plausible functional groups that are co-regulated: F_{kt} is a combination of Dynein and CENP-E-generated forces (Civelekoglu-Scholey et al., 2006), F_{dep}^{kt} is the force from depolymerizing kin-I kinesin, similar to Kinesin-13 at the pole, and F_{poly}^{kt} is the direct effect of ktMT polymerization force (Scholey and Mogilner, 2002). These functional groups are not independent of each other; specifically, F_{dep}^{kt} and F_{poly}^{kt} are mutually exclusive forces, and only one of them can be active at a time. These dependencies are incorporated into the switch parameters. We define a switch variable P_{mt} responsible for ktMT dynamics: in the presence of polymerization or depolymerization, $P_{mt} = 1$, while in the absence of both effects $P_{mt} = 0$. An additional switch, P_{poly} accounts for the actual type of the ktMT activity: $P_{poly} = 1$ when the force is generated by polymerization and $P_{poly} = 0$ when the force is generated by depolymerization. The activity of the kt motor is represented by the switch P_{kt}.

Similar to chrMTs, when there is no depolymerizer at the minus-end, we assume that the ktMT is anchored to the pole either by the inactive depolymerizing motor or by some other anchoring

protein. The movement rate of the kt motors is the rate of pole movement minus the kt movement rate, so that if both pole and kt move at the same rate in the same direction, the motor moves relative to the ktMT with zero speed. The resulting force based on the motors' force-velocity relations is:

$$F_4 = P_{kt}F_{kt,mx}\left(1+\frac{V_{pole}-V_{chr}}{V_{kt,mx}}\right)+P_{mt}\left(\left(1-P_{poly}\right)F_{dep}^{kt}\left(1+\frac{V_{pole}-V_{chr}}{V_{dep,mx}^{kt}}\right)-P_{poly}F_{poly}^{kt}\left(1-\frac{V_{pole}-V_{chr}}{V_{poly,mx}^{kt}}\right)\right) \quad (6)$$

where $V_{kt,mx}$, $V_{poly,mx}^{kt}$ and $V_{dep,mx}^{kt}$ are the unloaded motor velocities and $F_{kt,mx}$, F_{poly}^{kt} and F_{dep}^{kt} are the maximal forces for the kt, polymerization, and depolymerization motors on the kt, respectively.

1.4.2 With depolymerizer at the pole and force generators on the kt

In this case, the depolymerizer at the ktMT minus-end is active, and there are active motors on the kt. Therefore, we need to find the depolymerization velocity of the ktMT first by examining the force balance on the ktMTs at the minus-end and plus-end (left- and right-hand-side, respectively):

$$F_{dep,mx}\left(1-\frac{V_{speckle}^{kt}-V_{pole}}{V_{dep,mx}}\right)=P_{kt}F_{kt,mx}\left(1-\frac{V_{chr}-V_{speckle}^{kt}}{V_{kt,mx}}\right)+$$

$$+P_{mt}\left(\left(1-P_{poly}\right)F_{dep}^{kt}\left(1-\frac{V_{chr}-V_{speckle}^{kt}}{V_{dep,mx}^{kt}}\right)-P_{poly}F_{poly}^{kt}\left(1+\frac{V_{chr}-V_{speckle}^{kt}}{V_{poly,mx}^{kt}}\right)\right)$$

A straightforward (yet tedious) solution of this equation:

$$V_{speckle}^{kt}=\frac{\left(F_{dep,mx}\left(1+\frac{V_{pole}}{V_{dep,mx}}\right)-P_{kt}F_{kt,mx}\left(1-\frac{V_{chr}}{V_{kt,mx}}\right)-P_{mt}\left(\left(1-P_{poly}\right)F_{dep,mx}^{kt}\left(1-\frac{V_{chr}}{V_{dep,mx}^{kt}}\right)-P_{poly}F_{poly,mx}^{kt}\left(1+\frac{V_{chr}}{V_{poly,mx}^{kt}}\right)\right)\right)V_{poly,mx}^{kt}V_{dep,mx}^{kt}V_{kt,mx}V_{dep,mx}}{F_{dep,mx}V_{poly,mx}^{kt}V_{dep,mx}^{kt}V_{kt,mx}+P_{kt}F_{kt,mx}V_{poly,mx}^{kt}V_{dep,mx}^{kt}V_{dep,mx}+P_{mt}\left(1-P_{poly}\right)F_{dep,mx}^{kt}V_{poly,mx}^{kt}V_{kt,mx}V_{dep,mx}-P_{mt}P_{poly}F_{poly,mx}^{kt}V_{dep,mx}^{kt}V_{kt,mx}V_{dep,mx}} \quad (7)$$

allows calculating the force of a single ktMT from the following formula:

$$F_5 = F_{dep,mx}\left(1-\frac{V_{speckle}^{kt}-V_{pole}}{V_{dep,mx}}\right) \quad (8)$$

1.4.3 With depolymerizer at the pole but without force generation on the kt

In this case, only the depolymerizing motor is active, and we assume that the ktMTs are anchored at their plus-ends. Therefore the corresponding force is:

$$F_6 = F_{dep,mx}\left(1+\frac{V_{pole}-V_{chr}}{V_{dep,mx}}\right) \quad (9)$$

1.4.4 Total force

In the general case, for multiple ktMTs, we need to take into account all possible switch configurations. In the ktMT case, due to the dependencies between switches, the expression is more cumbersome than those for other MT populations; nevertheless, the concept is the same as before.

The total force is the product of the single ktMT force, F_4, F_5 or F_6, and of the number of ktMTs, N_{kt}:

$$F_{kt} = N_{kt}\left(\left(1-P_{dep}\right)\left(1-\left(1-P_{mt}\right)\left(1-P_{kt}\right)\right)F_4 + P_{dep}\left(1-\left(1-P_{mt}\right)\left(1-P_{kt}\right)\right)F_5 + P_{dep}\left(1-P_{mt}\right)\left(1-P_{kt}\right)F_6\right) \quad (10)$$

1.5 Force on ipMT population

There are two possible configurations for ipMTs: (i) sliding motors in the anti-parallel ipMT overlap zone at the spindle equator, without depolymerizing motors at the pole on the ipMT minus-ends, and (ii) sliding motors with depolymerizing motors. In both configurations, we assume that there is some 'protein friction' (Tawada and Sekimoto, 1991) caused by dynamic cross-linkers in the anti-parallel ipMT overlap zone at the spindle equator.

1.5.1 Without depolymerizer at the pole

The force on a single ipMT is generated by the action of Kinesin-5 and Kinesin-14 on the overlap region of length *L*, so without minus-end depolymerization, we have:

$$F_7 = P_{kin-5}LF_{61F,mx}\left(1-\frac{V_{pole}}{V_{61F,mx}}\right) - P_{Ncd}LF_{Ncd,mx}\left(1+\frac{2V_{pole}}{V_{Ncd,mx}}\right) - \xi L2V_{pole} \quad (11)$$

Here $V_{61F,mx}$, $V_{Ncd,mx}$ are the unloaded velocities, and $F_{61F,mx}$, $F_{Ncd,mx}$ are the maximal forces of Kinesin-5 and Kinesin-14, respectively. Different signs account for the fact that those are plus- and minus-end directed motors, respectively. The magnitude of the relative velocities between ipMT and the motors are different for Kinesin-5 $\left(V_{pole}\right)$ and Kinesin-14 $\left(2V_{pole}\right)$, since Kinesin-5 is a bipolar motor and moves along both ipMTs, and therefore is stationary relative to the lab frame of reference, whereas Kinesin-14 binds a single ipMT and moves along the other ipMT. The last term accounts for the viscous-like drag force produced by the dynamic cross-linkers. This force is proportional to relative sliding rate $2V_{pole}$ of anti-parallel ipMTs at the spindle equator, and ξ is the respective friction coefficient. Note that all forces are proportional to the length of the overlap region *L*, so we implicitly assume that the ipMT length is a limiting factor in the motors' numbers, and that there is a certain number of Kinesin-5, Kinesin-14, and cross-linkers per unit overlap length. Respective forces are per micron of the ipMT length. We also assume that the multiple motor forces on a single ipMT are additive.

1.5.2 With depolymerizer at the pole

In a similar fashion to chrMT and ktMT, if we define the relative velocity between a sliding motor and the ipMT it slides on as $V^{ip}_{speckle}$, we obtain that the balance of forces on a single ipMT is:

$$-P_{kin-5}LF_{61F,mx}\left(1-\frac{V^{ip}_{speckle}}{V_{61F,mx}}\right) + P_{Ncd}LF_{Ncd,mx}\left(1+\frac{2V^{ip}_{speckle}}{V_{Ncd,mx}}\right) + \xi L2V^{ip}_{speckle} = F_{dep,mx}\left(1-\frac{V^{ip}_{speckle}-V_{pole}}{V_{dep,mx}}\right)$$

Therefore, the velocity is:

$$V_{speckle}^{ip} = \frac{\left(P_{kin-5} LF_{61F,mx} - P_{Ncd} LF_{Ncd,mx} + F_{dep,mx} \left(1 + \frac{V_{pole}}{V_{dep,mx}} \right) \right) V_{61F,mx} V_{Ncd,mx} V_{dep,mx}}{P_{kin-5} LF_{61F,mx} V_{Ncd,mx} V_{dep,mx} + 2P_{Ncd} LF_{Ncd,mx} V_{61F,mx} V_{dep,mx} + 2\xi L V_{61F,mx} V_{Ncd,mx} V_{dep,mx} + F_{dep,mx} V_{61F,mx} V_{Ncd,mx}} \quad (12)$$

and the force is:

$$F_8 = -F_{dep,mx} \left(1 - \frac{V_{speckle}^{ip} - V_{pole}}{V_{dep,mx}} \right) \quad (13)$$

1.5.3 Total Force

Again, the total force is the product of the single ipMT force and the number of ipMTs. Similar to asMTs, we assume that there are two possible ipMT numbers: N_{ovrlp}^{high} and N_{ovrlp}^{low}, and we assign a switch parameter P_{ovlp} to control this number. The total force on a single motor is:

$$F_{ip} = \left(P_{ovlp} N_{ovrlp}^{high} + \left(1 - P_{ovlp} \right) N_{ovrlp}^{low} \right) \left(\left(1 - P_{dep} \right) F_7 + P_{dep} F_8 \right) \quad (14)$$

The overlap length is one of the model dependent variables. It changes over time following a simple kinematics equation (Brust-Mascher et al., 2004):

$$\frac{dL}{dt} = 2V_{poly}^{ip} - 2\left(\left(1 - P_{dep} \right) V_{pole} + P_{dep} V_{speckle}^{ip} \right)$$

where V_{poly}^{ip} is the ipMT plus-end polymerization velocity.

1.6 Chromosome and Pole movement

1.6.1 Chromosome movement

The algebraic equations (1-15) provide the total force on all four MT populations in the spindle. Here, we combine these forces to analyze how the distance between sister chromatids changes over time. Two out of four MT populations' forces are applied to the chromosomes, so *D*, the distance between the sister chromatids, is increased by the sum of these two forces and the force of cohesion between the sister chromatids:

$$\frac{\mu_{chr}}{2} \frac{dD}{dt} = F_{kt} - F_{chr} - F_{cohesion}$$

Here μ_{chr} is the effective viscous drag coefficient of the chromatid. Note, that the equation of motion is based on low Reynolds number hydrodynamics conditions in the cell (Scholey and Mogilner, 2002), therefore the velocities of all objects in the cell are proportional to forces applied to them. The signs of forces are due to the fact that the ktMT force pulls chromatids outward, while the chrMT force pushes them inward assisted by the cohesion. Total kt and chromosome arm forces are defined above (5,10), and we define the cohesion force as a simple linear spring:

$$F_{cohesion} = P_{cohesion} \beta \left(D - d_0 \right) \quad (15)$$

where d_0 is the cohesion spring rest length, β is its spring constant, and $P_{cohesion}$ is the cohesion switch which is equal to one before anaphase, and is equal to zero at the anaphase onset when the cohesion between the sister chromatids is dissolved.

1.6.2 Pole movement

Similarly, based on the same low Reynolds number approximation, the rate of pole separation is given by the following equation:

$$\frac{\mu_{pole}}{2}\frac{dS}{dt} = F_{ip} + F_{chr} + F_{aster} - F_{kt}$$

where μ_{pole} is the effective viscous drag coefficient associated with the pole movement, and the right hand side is the sum of all MT populations' forces applied to each pole (interpolar, astral, and chromokinesin forces push the poles apart, while the kt force pulls them together).

1.7 Final set of equations and their numerical solution.

The final set of differential equations of the model is:

$$\frac{\mu_{pole}}{2}\frac{dS}{dt} = F_{ip} + F_{chr} + F_{aster} - F_{kt} \quad (16)$$

$$\frac{\mu_{chr}}{2}\frac{dD}{dt} = F_{kt} - F_{chr} - F_{cohesion} \quad (17)$$

$$\frac{dL}{dt} = 2V_{poly}^{ip} - 2\left(\left(1 - P_{dep}\right)V_{pole} + P_{dep}V_{speckle}^{ip}\right) \quad (18)$$

$$V_{pole} = \tfrac{1}{2}\frac{dS}{dt} \quad (19)$$

$$V_{chr} = \tfrac{1}{2}\frac{dD}{dt} \quad (20)$$

complemented by the algebraic equations (1-15).

These differential-algebraic equations are then solved numerically using stiff SUNDIALS' IDA solver (http://www.llnl.gov/casc/sundials/). Representative models were additionally solved using Matlab's *ode15s* stiff solver for comparative purpose to test solver accuracy and performance. In cases of numerical instability, a penalizing score was assigned. Finally, to determine if a model is a sufficient fit to the experimental data, a manually selected predefined cutoff was used. To account for the motors' on and off switching, after the up to 11 times at which the switching occurs are chosen by the computer, the whole time domain is divided by these times into up to 12 sections within each of which the model parameters stay constant. The equations were then solved separately for each section, where the solutions at the end of each section were used as the next section's initial conditions. Note, that this partitioning is different for each individual model, and that the duration of the sections is completely random in principle.

Supplementary table of parameters

Symbol	Meaning	Units	Possible Values / Range
P_{dep}	Kinesin-13 activity	Number	switch
P_{chr}	Chromosome arm motor activity	Number	switch
P_{dyn}	Dynein activity at the cortex	Number	switch
P_{kin-5}	Kinesin-5 activity	Number	switch
P_{Ncd}	Kinesin-14 activity	Number	switch
P_{kt}	kt motor activity	Number	switch
P_{mt}	ktMTs activity on the kt.	Number	switch
P_{poly}	Polymerization activity of ktMT	Number	switch
P_{as}	Level of astral MTs	Number	switch
P_{ovrlp}	Level of overlapping MTs	Number	switch
$P_{cohesion}$	Activity of the cohesion spring	Number	switch - fixed
β	Spring constant for cohesion	[pN/μm]	[500,5000]
d_0	Sister chromatid rest length	[μm]	[0.1, 2]
$F_{61F,mx}$	Kinesin-5 maximal load force per 1 μm of MT length	[pN/μm]	[1,100]
$F_{ncd,mx}$	Kinesin-14 maximal load force per 1 μm of MT length	[pN/μm]	[1,100]
$F_{dep,mx}$	Kinesin-13 maximal load force	[pN]	[1,10]
$F^{kt}_{dep,mx}$	kt depolymerization maximal force	[pN]	[1,10]
$F^{kt}_{poly,mx}$	kt polymerization maximal force	[pN]	[1,10]
$F_{dyn,mx}$	Dynein maximal load force	[pN]	[1,10]
$F_{kt,mx}$	kt motor maximal load force	[pN]	[1,10]
$F_{chr,mx}$	Chromokinesin maximal load force	[pN]	[1,10]
$V_{61F,mx}$	Kinesin-5 free load velocity	[μm/sec]	[0.01 0.1]
$V_{chr,mx}$	Chromokinesin free load velocity	[μm/sec]	[0.01 0.1]
$V_{dep,mx}$	Kinesin-13 free load velocity	[μm/sec]	[0.01 0.1]
$V^{kt}_{dep,mx}$	kt depolymerizing motor free load velocity	[μm/sec]	[0.01 0.1]
$V^{kt}_{poly,mx}$	ktMT polymerization free load velocity	[μm/sec]	[0.01 0.1]
$V_{kt,mx}$	kt motor free load velocity	[μm/sec]	[0.01 0.1]
$V_{ncd,mx}$	Kinesin-14 free load velocity	[μm/sec]	[0.01 0.1]
V^{ip}_{poly}	Polymerization velocity of ipMTs	[μm/sec]	[0.01 0.1]
μ_{chr}	Chromosome drag coefficient	[pN sec/μm]	[5 50]

μ_{pole}	Pole drag coefficient	[pN sec/μm]	[50 500]
N_{as}^{high}	High value of asMT number	Number	[50,500]
N_{as}^{low}	Low value of asMT number	Number	[5,50]
N_{ovrlp}^{high}	High value of overlapping ipMT number	Number	[50,500]
N_{ovrlp}^{low}	Low value of overlapping ipMT number	Number	[5,50]
N_{chrk}	Number of chrMTs	Number	[50,500]
N_{kt}	Number of ktMTs	Number	[50,200]
ξ	Cross-linkers friction coefficient density	[pN sec/μm^2]	[0 10]
A_{chr}	Chromosome area	[μm^2]	[10 250]

Supplementary Table 1 This table shows 39 parameters that represent the 'model parameter space'. In the first column are the symbols used in the mathematical equations above. The second column provides a brief description of each parameter. The third column shows the units for each parameter, and the last column shows the range for each parameter that was allowed during the stochastic optimization process. The parameter ranges were chosen based on the following considerations. Cohesion spring constant is of the order of magnitude characteristic for protein elasticity (Howard, 2001). Cohesion rest length is of the order of magnitude of the values ~1 μm observed experimentally (Goshima et al. 2005). All motor forces were assumed to be in a pN range, which is known for several motors similar to *Drosophila* mitotic motors (Scholey and Mogilner, 2002). Motor force densities for motors acting at the overlap between anti-parallel MTs are based on the same range for the force of an individual motors, and an assumption that there is ~ 10 motors per μm, supported by a number of observations (Sharp et al. 1999; Tao et al. 2006). Range for the motor velocities is of the order of magnitude of those measured for a few mitotic motors (Tao et al., 2006). Drag coefficients are of the orders of magnitude estimated in (Cytrynbaum et al., 2003). MT numbers are of the orders of magnitude estimated from the EM data (Mastronarde et al., 1993; McDonald et al., 1992). Order of magnitude of the cross-linkers friction coefficient density is estimated in (Tao et al., 2006). Estimates for the chromosome area are available from (Marshall et al., 2001).

2. Computational search in 'model space'

2.1 Experimental data and scoring individual models

We collected the experimental data for the scoring from the literature and unpublished data collected in our lab (supplementary table 2; SupFig. 1). To facilitate the comparison between the experiments and simulations, the experimental data was smoothed and aligned. To smooth the data, a piece-wise polynomial (spline) with 10-15 points was fitted to the data. The spline was re-sampled to get 55 points (from 0 to 278.3 seconds at 5.15 seconds intervals) generating a uniform time spacing for all different measurements. All experimental plots were aligned relative to the timing of the nuclear envelope breakdown and the timing of the slope change in prometaphase elongation. Interestingly, the anaphase B elongation that was not used for alignment, aligned well between different experimental curves providing an external validation for the alignment procedure.

Experiment	Reference
WT pole and chromosome separation	(Sharp et al., 2000); This work
Dynein – antibody injection	(Sharp et al., 2000)
Kinesin-5 antibody injection	(Sharp et al., 2000); This work
Kinesin-13 antibody injection	(Rogers et al., 2004)
Kinesin-14 null	(Brust-Mascher and Scholey, 2002)
Kinesin-5 antibody injection, Kinesin-14-null background	(Sharp et al., 2002); This work

Supplementary Table 2 References for the experimental data that were used for the optimization and that are presented in Fig 1c.

In the previous section, we derived a general mathematical model for spindle elongation and chromosome segregation during mitosis. These equations, together with the set of parameters, represent a very large set of potential models, each of them being a putative mechanistic explanation for spindle development in *Drosophila* embryo. Here we describe the computational search performed in that model parameter space in order to identify models that are in good agreement with the experimental data.

The computational search was done by combining repeated stochastic optimization and clustering. The problem of finding good models can be represented as an optimization problem, in which the objective function is the goodness of fit to the experimental data. Since the possible number of models that are a good fit to the experimental data is high, we repeated the optimization thousands of times to exhaustively explore the solution space. Comparison to the data was done based on the sum square of error criteria (SSE) between the data for the spindle length and/or chromosome separation time series and the model simulation results (measured in microns) over a discretized grid of 55 time points. In addition to SSE to the original pole (or chromosome) separation data, we found that using the SSE of the separation velocity of separation (the first derivative) substantially improves the optimization. The derivative residuals were scaled (×100) to have similar magnitude as the pole separation data. To allow the use of the derivative of the experimental data (which is noisy), we first smoothed and aligned the data using spline interpolations (SupFig. 1). The SSE between the smoothed derivative of the experimental data and the model prediction (measured in microns per second) and scaled as described above, was added to the SSE of the spindle length (with dimensions

'stripped' off), and the sum was used as a numerical score for the model. In addition, for the WT data, the SSEs for the inter-chromosomal distance and scaled derivative of this distance were added to the score. Based on visual inspections of thousands of fits, a cut-off score was determined. Fits below this cut-off score were accepted as adequate, whereas those above it were regarded as inadequate. This threshold was unique to each WT or inhibition dataset, and a model to be accepted, it would have to produce good fits for all datasets separately. The thresholds for the SSE (sum of the pole separation in microns and its weighted (×100) derivative in microns per second with stripped off dimensions) were: WT: 5 (including in addition, chromosome separation data), Kinesin-5: 2.2, Kinesin-14 1.5, Kinesin-13: 3, Dynein: 3 and the double inhibition Kinein-5 and Kinein-14: 4.5.

As expected, many of the independent optimization runs yielded very similar models. Therefore, we performed an additional clustering step that identified distinct groups of models that are biologically different and in good agreement with experimental results. Finally, we analyzed the search and demonstrated that it was saturated, i.e. we identified all major groups of distinct strategies for pole separation in the *Drosophila* embryo.

The computational search described here was repeated six times, each time with increasing amount of experimental data (Fig 1c and SupFig. 2). The computational procedure described is a single iteration of the search.

2.2 Optimization

The optimization process searched for models (points in the multi-dimensional model space) such that their numerical solutions are in good agreement with the experimental data. The description of the optimization process is organized as follows: We first define the objective function that was used to compare the simulation results and experimental data. The objective function assigns a score for a point in the model space based on the agreement of the solution of a corresponding model with the experimental data. Then, we describe the optimization algorithms that were used to identify points in the model space that are in good agreement with experimental data, i.e. they are local minima of the objective function. Finally, we describe the extension of the model space to include additional inhibition parameters and an improvement of the optimization algorithm to deal with those additional parameters. Those additional parameters allow simulation of both WT and inhibition cases and their comparison to the experimental data.

2.2.2 Genetic Algorithm

The objective function assigns a goodness-of-fit score to the results of the numerical solution of each model (a smaller score is a better fit to the experimental data). To identify models that provide a good fit and could potentially explain the experimental results, we used a genetic algorithm approach (Mitchell, 1996). The genetic algorithm mimics the process of evolution where a population of solutions evolves by mutation, recombination and selection toward a minimal value of the objective function. Specifically, in our case this means that 'successful' models encoded by the set of model parameters, both changed their parameters randomly (mutation), exchanged values of the parameters with each other (recombination), and were accepted or rejected based on the scores (selection). The optimization was done with a custom Matlab code that was adapted based on the GEATBX package (http://www.geatbx.com/docu/index.html). The following operators were used in the optimization:

Mutation: Mutation scheme followed the Breeder Genetic Algorithm scheme.

Recombination: Two separate recombination operators were used for switch and mechanical/kinetic parameters. For non-switch (mechanical / kinetic) parameters, a recombination event was as follows: First, for each parameter, a random number δ between -0.2 to 1.2 was chosen. Then, the new parameter value was calculated using the following formula: $C=\delta\times P_1+(1-\delta)\times P_2$ where C is the new 'offspring' parameter value and P_1 and P_2 are the values of the parameter in two recombined 'parent' models. For switch parameters, a variant of the above calculation was used due to the 'circular' nature of the switch parameters (i.e. turning a switch off at t=0 or turning it on at t=278.3 seconds have the same biological meaning). The two parent models were placed on a circle using the periodic boundary condition. The pairs of parent models always defined two arcs that separate them on the circle. The recombination happened on the shorter of the two possible arcs using the same formula as the one for the non-switch parameters.
Migration: The population was divided into 20 subpopulations, each comprised of 50 individuals. Every 10 generations, 20% of the populations were mixed randomly.
Selection: Selection was performed using Roulette Wheel Selection with 80% new individuals inserted at each generation.

2.2.3 Multiple-objective optimization

To test whether a specific model fits not only the WT data, but also the data from different experimental perturbations, we extended the optimization process to allow scoring by comparing multiple simulations to multiple experimental conditions. To do so, we extended the model to include additional parameters that are specific to the different experimental conditions. These parameters all encode the extent of inhibition by antibody injection. In addition to extending the model space, we also solved the equations multiple times for each one of the inhibition datasets.

2.2.4 Using the switch parameters to mimic biochemical inhibitions

The optimization process described above compared a single simulation run to experimental data from WT pole separation and chromosome segregation curves. We extended that optimization process to identify points in the model space that are also a good fit to the experimental data, where a specific force generator was inhibited either genetically or biochemically using antibody injections. The specific datasets used are described in supplementary table 2. To allow a comparison between the model and those additional datasets, the model was 'inhibited' by lowering the maximal value of the activity of the switch that corresponds to the molecular identity of the inhibited force generator. We considered null mutant data (Kinesin-14-null embryo) as complete inhibition, i.e. Kinesin-14 activity was always zero regardless of its switching behavior. For inhibitions that were a result of an antibody injection, an additional parameter that determines the extent of inhibition was added to the optimization, increasing the dimensionality of the model space. Overall, 7 additional parameters were used, increasing model space dimensionality from 38 to 45. To compare the model and experimental data, the model equations were solved nine times for WT and all inhibition experiments. The overall objective function score was the weighted sum of these nine simulations and included pole separation curves and their derivatives.

2.2.5 Deterministic improvement

In addition to the stochastic optimization described above, we included a deterministic gradient descent step that helped to improve the fit to the experimental data in cases where multiple pole separation curves were used. The deterministic optimization was done in Matlab using the optimization toolbox. The specific improvement was done in two steps: first, a multi-parameter

optimization using Matlab's *fminsearch* function that uses a simplex-based algorithm was used. Then, to fine-tune fits to all mutant curves, a single parameter optimization was performed for each of the additional inhibition parameters using Matlab's *fminbnd* function that is based on golden section search and parabolic interpolation. A sample plot shows the evolution of the optimization score in SupFig. 2a. The plot shows both stochastic and deterministic portions of the optimization. The stochastic portion required ~240 min, whereas the deterministic improvement required ~20 min of CPU time.

2.3 Clustering

Clustering was used to identify groups of models that are qualitatively different from one another. The optimization process was repeated thousands of times to explore different regions in the model space. Many of the successful optimization runs yielded models that were very similar to each other, while others were qualitatively different. To identify all groups of essentially different models, we performed clustering procedure as follows: First, we defined a distance measure between any two models. Second, we used standard hierarchical clustering to build a linkage tree of all models. Finally, we used a convexity criteria to recursively identify distinct models in the hierarchical tree.

2.3.1 Distance measure

To be able to cluster models into distinct groups it is necessary to have a measure that can identify how similar two models are. There are two types of parameters, defined in supplementary table 1: switch and kinetic/mechanical parameters. Both types determine the forces that are acting on the MT populations. The sum of these forces is what drives pole separation. Biologically similar models have similar force dynamics, whereas biologically dissimilar models are characterized by essentially different force dynamics. Therefore, we used combined forces' difference as a natural measure of the models' similarity. Specifically, the square root of the time-average square of the differences between all 4 MT populations' forces predicted by a pair of models was used as a measure of distance between these two models. In addition, since we identified cases in which models that were different biologically still gave a similar force profile, we added an additional measure: the square root of the average square difference between all switches. The overall distance measure is the sum of the difference between the forces and the difference between switches appropriately weighted to have similar magnitude. For the nonlinear scaling and dimensionality reduction in Fig. 2g,e, we used the Matlab statistical toolbox command *mdscale* with default parameters based in the dissimilarity matrix that was later used for clustering. Metric multidimensional scaling is an optimization-based method that identifies a lower dimensional representation of the data that maximizes the similarity between the distance matrix in the low dimensions and the original distance matrix.

2.3.2 Linkage analysis

Given a dissimilarity matrix between all pairs of models, a linkage analysis was performed to determine the hierarchical tree. The linkage was calculated using standard statistical procedure, the furthest distance method.

2.3.3 Dividing into clusters

We developed a criterion to identify a set of models that are from the same cluster. The criterion was inspired by the definition of a biological species which is defined as having a reproductive

barrier. This criterion was then applied to the hierarchical tree in a recursive fashion to identify distinct groups of models that are different from one another.

2.3.3.1 Clustering criterion

We reasoned that if a set of models forms a distinct cluster, then combinations of models from this cluster should also be a good fit to the experimental data. In practice, we generated 1000 new models that are all combinations of the old models by using a convex sum of the parameters: $C=\delta\times P_1+(1-\delta)\times P2$ where $0<\delta<1$. We then scored all those new 1000 models using the objective function as described above. If the median of the 1000 new scores was smaller than the cutoff used for evaluating models, we considered the set of models a distinct cluster. The mathematical implication of this criterion is that models are expected to be topological convex sets in the parameter space. This is a reasonable assumption given the convex nature of the force balance relations in the models. An illustration of the clustering criterion is shown in SupFig. 2b. In that figure, a hypothetical 2-dimensional fitness landscape is shown. There are two peaks in the landscape that are above a threshold; they are considered a good fit. The figure shows two pairs of good models; in one pair, the line that connects them is crossing a 'valley', and as a result, models on this line will not be considered 'viable progenies'. However, the line connecting the two models that are on the same peak will correspond to the models producing good fits, and therefore will be considered belonging to the same group.

2.3.3.2 Identifying clusters on a tree

Using this clustering criterion and the hierarchical tree, we identified distinct clusters by a recursive descend on the tree, where in each node we determined whether the set of models below that node is a distinct cluster based on the above criteria. The natural stopping condition for the recursion was either identification of a cluster, or a 'terminal leaf' – a cluster consisting of a single model.

2.3.4 Improvement of clustering robustness

The clustering methodology described above depends heavily on the topology of the hierarchal tree. We observed that, as is the case in other usages of hierarchical clustering, the topology of the tree can change substantially with a small change in the population of models that are tested. To improve the robustness of the clustering, we used an ensemble method. In general, ensemble methods cluster sets of variables based on several clustering variants and determine the final grouping based on a consensus between all clustering variants (Topchy et al., 2004).

Ensemble clustering: to generate cluster variants, we used a re-sampling approach. We re-sampled 20 new sets of models by a 'jackknife' procedure that randomly chose 95% of the models and generated a clustering assignment for the subset of models. Each subset was clustered using the same clustering procedure as above.

Choosing consensus clustering: To choose the final clustering, we chose the best 'consensus' cluster out of the 20 sets where the 'consensus' clustering was defined as the clustering that has the best agreement with the rest of the 19 clustering possibilities.

2.4 Convergence analysis

We performed six searches in the model space, using WT data only and using increasing amount of experimental datasets (Fig 2c and supplementary table 2). To determine that the search for models was exhaustive, we used a re-sampling approach. We re-sampled smaller sets of models and clustered them as described above. The result of the number of clusters as a function of the sample

size is shown in SupFig. 2c. If the search converges, then increasing the sample size should not increase the total number of model groups. However, if the search is far from convergence, then as we increase the sample size, the number of identified clusters should increase. This problem is analogous to a problem in ecology, where the number of species in a habitat is estimated (Chao and Bunge, 2002). As can be seen in SupFig. 2c, all re-sampling datasets follow the expected hyperbolic curve. It is computationally prohibitive to reach saturation for all datasets, therefore we focused our attention at the final stage that includes all the experimental data and reach saturation at six groups (SupFig. 2c, SupFig. 3 and Fig. 3).

3. Additional results

3.1 Demonstration of the fit to experimental data for a representative model

In SupFig. 4, we show a representative model from group 1. Panel a shows the fit where panels b-f give the parameters value for this model. Similar figures can be easily generated for other plausible models or for any specific hypothesis or data from future experiments.

3.2 Chromosome separation after inhibition

It is interesting to note that different model groups did not differ regarding their predictions of chromosome separation after the different types of inhibitions. This observation is notable for two reasons. First, it suggests a level of robustness in chromosome separation. As long as the poles separate, so do the chromosome, and in inhibitions that increase the rate of pole separation, chromosome separation is mostly unaltered. In addition, this demonstrates that not all new experimental data would be useful to further constrain the six model group and that rational experimental design is necessary.

3.3 Virtual Speckle analysis

As an intermediate step in the calculation of pole separation over time, the mathematical formulation requires calculating the velocities of single MTs in the different MT populations. It is interesting to examine these velocities, since they can be compared to experimental data. Fluorescence speckle microscopy allows measurement of MT velocities by tracking speckles of the fluorescence marker over time (Danuser and Waterman-Storer, 2006). SupFig. 5 shows the median speckle velocity on all three (besides astral) MT populations in a set of ~200 representative models from the last iteration of the optimization. This analysis shows that the three different MT populations undergo different dynamics. ipMTs show high levels of velocities that peak when the spindle elongates. chrMTs show profiles similar to ipMTs until anaphase A, but unlike ipMTs, they do not change their profile in either anaphase A or B. ktMTs show lowest levels of velocities to the extent that the MT velocity decreases to zero during metaphase. This prediction is not supported by the experimental data (Sharp et al., 2000; Brust-Mascher and Scholey 2002); however, since the experimental distinction between the three MT populations is very challenging experimentally, it is hard to make specific assertions regarding this apparent disagreement between the experimental and simulation results. Another indication for this disagreement can be seen in SupFig 5 showing the predicted MT speckle velocity for all models of the final search iteration. The histogram shows a small variation with an average value of 0.02 μm/sec. Experimental measurements show a much higher variability and a higher average of 0.06 μm/sec (Brust-Mascher et al., 2004). These discrepancies are resolvable, and are likely a result of the model limitations. The modeling framework assumes that all MTs in a single population are identical without taking individual MT dynamic instability into account. A specific formulation of multiple individual MTs was too computationally intensive to allow a search in parameter space.

3.4 Slow maximal velocity of Kinesin-13

Analysis of Kinesin-13 shows that the maximal velocity is tightly conserved and is of small magnitude. However, the maximal force is not much different from that generated randomly (p-value > 0.8, t-test). There is no correlation between the maximal force and unloaded velocity ($r = -0.01$). This supports the notion that the spindle is robust to the magnitude of the maximal force, and

its actual value is insignificant for the spindle elongation. This is in sharp contrast to the maximal velocity that seems to be sensitive to changes in parameter values and is tightly conserved.

3.5 Activity profiles – switch parameters

The mathematical formulation of models includes 11 switch parameters that can change the molecular activity once over the course of time from prometaphase till end of anaphase. Out of these 11 switches, the cohesion switch was set to turn off at T=178 sec, when chromosomes start to segregate. All other 10 switches were not predefined, and the optimization process determined the exact timing of those switches. From the 10 remaining switches, 4 show highly conserved values among all models, suggesting that they represent the essential unique activity in the spindle. Of the other 6 switches, 2 exhibit a bi-model histogram suggesting two alternative biological scenarios, and 4 others have multi-modal distributions that can either suggest that the spindle is robust to the biological feature represented by these parameters, or alternatively that our analysis was unable to determine the correct model due to lack of appropriate experimental data. SupFig. 6 shows the activity of the switch parameters and the resulting forces for all models at all search iterations. As the amount of experimental data is increased, the number of possible values for the switching time decreases. Here we describe a few of those conserved switch parameters and their biological significance.

3.5.1 Pole depolymerization, Kinesin-13 (Klp10A)

Previous experimental and computational work (Brust-Mascher and Scholey, 2002; Brust-Mascher et al., 2004) demonstrated that spindle elongation during anaphase B is a result of a switch in pole depolymerization activity. During metaphase and anaphase A, the MTs are depolymerized at the pole, which causes net MT flux (Rogers et al., 2005). At the onset of anaphase B, MT depolymerization at the spindle pole end (Brust-Mascher and Scholey, 2002) causes the MTs to push the poles and elongate the spindle. In all models in the sixth iteration (SupFig. 6), the activity of the pole depolymerizer is tightly regulated.

3.5.2 Inter-polar MT force generators, Kinesin-5 (Klp61F) and Kinesin-14 (Ncd)

Previous experimental studies identified Kinesin-5 as a bipolar kinesin that is capable of sliding MTs (Kapitein et al., 2005) and is localized to the anti-parallel ipMT overlap zone (Sharp et al., 1999). In a variety of different organisms, this motor was shown to be important for mitotic progression (Cole et al., 1994; Cottingham et al., 1994; Enos and Morris, 1990; Heck et al., 1993; Saunders and Hoyt, 1992; Hoyt et al., 1992; Sawin et al., 1992; Straight et al., 1998). Inhibition of Kinesin-5 causes poles' collapse in a variety of organisms further supporting its role as an outward force generator. We found that in all models of the final iterations (SupFig. 6), Kinesin-5 is up-regulated in the late prometaphase. Kinesin-5 is antagonized by Kinesin-14 (Tao et al., 2006; Sharp et al., 1999). We found that in all these models, Kinesin-14 is up-regulated during the transition from prometaphase to metaphase. The temporal change in the two regulatory events suggests a mechanism for prometaphase elongation where only the outward motor (Kinein-5) is active. When Kinesin-14 starts working, the elongation is stopped as well causing the metaphase steady state. In our model the activity of Kinesin-14 lasts till the end of mitosis.

The predicted activity profile of Kinesin-14 is slightly different from the one that was inferred in previous experimental work (Brust-Mascher and Scholey, 2002; Sharp et al., 2000). The two main

differences are in late prometaphase and anaphase B. In late prometaphase in the models, Kinesin-5 works without Kinesin-14 antagonism, while interpretation of the experimental data suggests otherwise. In anaphase-B, Kinesin-14 is active in the model, but is thought to be inactive in the actual spindle. The latter discrepancy is easy to resolve. In this case, since the model only allows a single switch per motor, and Kinesin-14 "used up" its switch already at an earlier mitotic stage, it is not allowed to go through a second regulatory transition. In the model, these results in the pole separation slope in anaphase-B in WT embryo being different from that in Kinesin-14 null embryos (see SupFig. 4a). This difference in the slopes does not exist in the experimental data; in fact, this difference in the slopes is the only failure, in which the simulation fails to reproduce the experimental data. This supports the claim that Kinesin-14 is inactive during anaphase-B and shows the limitations of this modeling framework. This limitation – only one switch per motor – is hard to overcome due to an enormous increase in the number of possibilities that allowing multiple switches per motor would generate. However, this can also be looked at as a power of the search: a negative result, i.e. the inability to fit the anaphase-B slope, demonstrated that one of the model assumptions is probably incorrect.

The second discrepancy – the activity of Kinesin-14 during prometaphase – is not resolved. Further computational and experimental work is needed to identify the source of this discrepancy. A possible reason is that other motors and/or cross-linking proteins that were not modeled explicitly and were not assigned specific switch parameters go through regulatory transitions, and the activity profile identified by the computational search is an approximation for those multiple factors.

3.5.3 Astral MT force generators, Dynein

Dynein motors acting on the cortex are thought to generate pulling forces on the poles and participate in pole separation. Inhibition by antibody injection into the early Drosophila embryo prevented prometaphase elongation (Sharp et al., 2000). Consistent with these findings, our computational analysis shows that in all models resulting from the final search iteration (SupFig. 6), Dynein is active in prometaphase, and its activity is being down-regulated during the end of prometaphase elongation and the beginning of metaphase. Interestingly, the exact timing of Dynein down-regulation seems to be less conserved compared to the other three motors (SupFig 6a-c). Two possible explanations to this wider distribution are: (i) The step-wise switch approximation is inaccurate, and in fact Dynein's down-regulation takes place over ~ 50 second. (ii) There is a polymorphism in Dynein's activity, different embryos and even different spindles within the same embryo might down-regulate Dynein at different times and still exhibit a similar pole separation phenotype.

3.5 Activity profiles – switch parameters

The ultimate quantitative results of the search are the parameter value distributions for the six model groups shown in SupFig. 6. In addition, the average parameter values are gathered in the supplementary table 3.

Group # / Param.	1	2	3	4	5	6
P_{dep}	-0.21339	-0.21176	-0.21576	-0.21619	-0.21511	-0.215
P_{chr}	-0.4756	-0.04609	-0.10268	0.38919	-0.03027	-0.07024
P_{dyn}	-0.71909	-0.72415	-0.74943	-0.79578	-0.73496	-0.77101
P_{kin-5}	0.074206	0.059334	0.069793	0.06712	0.073361	0.069085
P_{Ncd}	0.25383	0.23307	0.24478	0.24487	0.25998	0.26664
P_{kt}	0.15301	0.12363	-0.07524	0.05904	0.005275	-0.02041
P_{mt}	0.38487	0.10252	0.094426	-0.3726	-0.78127	0.60356
P_{poly}	0.39893	-0.0901	-0.68795	-0.4988	-0.38425	-0.54832
P_{as}	0.48194	-0.38489	0.60931	0.55908	0.59661	0.59807
P_{ovrlp}	-0.2184	-0.17327	-0.17482	-0.22563	-0.16763	-0.13945
$P_{cohesion}$	-0.38	-0.38	-0.38	-0.38	-0.38	-0.38
β	4465.8	4052.2	4544.9	3980.2	4322.2	4388.7
d_0	0.91947	0.83379	0.93163	0.91567	0.93932	0.92677
$F_{61F,mx}$	64.273	65.419	66.139	67.409	64.725	66.88
$F_{ncd,mx}$	10.894	9.0618	10.584	9.8751	11.365	12.756
$F_{dep,mx}$	5.144	6.6178	6.6383	6.2448	6.744	5.2918
$F^{kt}_{dep,mx}$	5.2942	5.3704	6.0726	5.2791	5.2149	5.6327
$F^{kt}_{poly,mx}$	4.9669	5.2208	5.3736	6.4934	6.2738	5.1811
$F_{dyn,mx}$	6.5897	3.4108	7.1749	6.8242	6.1525	8.366
$F_{kt,mx}$	6.7091	6.5411	5.6165	5.8757	5.6024	5.9444
$F_{chr,mx}$	4.2893	4.2044	3.966	3.8222	3.9296	4.0275
$V_{61F,mx}$	0.033661	0.030423	0.029943	0.030879	0.0331	0.034898
$V_{chr,mx}$	0.048789	0.035911	0.045173	0.016966	0.038036	0.037935
$V_{dep,mx}$	0.014563	0.013846	0.013187	0.014288	0.014768	0.014956
$V^{kt}_{dep,mx}$	0.050058	0.037377	0.02842	0.042479	0.051354	0.0118
$V^{kt}_{poly,mx}$	0.040317	0.047747	0.046817	0.044596	0.051777	0.044893
$V_{kt,mx}$	0.042136	0.036948	0.03992	0.041582	0.025197	0.049582
$V_{ncd,mx}$	0.060667	0.059003	0.0623	0.061003	0.061039	0.059122
V^{ip}_{poly}	0.028411	0.029958	0.029687	0.028757	0.028892	0.028284
μ_{chr}	30.23	29.108	35.031	22.888	31.641	33.725
μ_{pole}	301.47	262.18	170.39	322.97	268.57	252.21

N_{as}^{high}	219.2	189.57	230.23	212.94	247.31	229.28
N_{as}^{low}	37.3	27.056	39.22	34.902	35.717	41.202
N_{ovrlp}^{high}	365.16	401.76	390.48	319.91	347.32	349.4
N_{ovrlp}^{low}	26.234	25.866	25.728	26.496	25.218	26.82
N_{chrk}	217.93	224.78	210.26	194.03	186.76	198.29
N_{kt}	108.46	118.15	113.52	110.35	115.48	106.26
ξ	5.388	5.0907	5.396	5.9555	5.7317	5.2909
A_{chr}	102.72	102.38	92.196	114.93	85.135	95.25

Supplementary Table 3 Average parameter values for the identified six model groups.

4. Model assumptions and limitations

The model is based on the following assumptions:

- the spindle has a mirror symmetry about the equator;

- the spindle is effectively one-dimensional, and MT elasticity does not contribute to the force balance;

- all motors are homogenously distributed in the spindle, and it is the MT lengths, not the motor concentrations, that are limiting factors in the numbers of the working motors;

- there is no dependence of motor affinity on the generated forces;

- only binary variations of the motor activities and MT numbers are allowed;

- the multiple motor forces are additive;

- only one switch per motor is allowed;

- force-velocity relations characterizing the motors are linear.

Some of these assumptions (mirror symmetry of the spindle) are reasonable based on the observations. Others are reasonable from theoretical considerations (i.e., one-dimensional character of the model is likely adequate for the rough force balance). Yet others are widely accepted in the literature, and probably not very critical (additive motor forces and linear force-velocity relations). Changing of some of the assumptions, made here for the sake of tractability, would probably significantly change the results (i.e., homogenously distribution of motors, no dependence of motor affinity on force, only binary variations of MT numbers, only one switch per motor). At this point, it is rather difficult to assess how this formidable combination of assumptions can affect adequacy of our model.

References

Brust-Mascher, I., Civelekoglu-Scholey, G., Kwon, M., Mogilner, A., and Scholey, J.M. (2004). Model for anaphase B: role of three mitotic motors in a switch from poleward flux to spindle elongation. Proceedings of the National Academy of Sciences of the United States of America *101*, 15938-15943.

Brust-Mascher, I., and Scholey, J.M. (2002). Microtubule flux and sliding in mitotic spindles of Drosophila embryos. Molecular biology of the cell *13*, 3967-3975.

Chao, A., and Bunge, J. (2002). Estimating the number of species in a stochastic abundance model. Biometrics *58*, 531-539.

Civelekoglu-Scholey, G., Sharp, D.J., Mogilner, A., and Scholey, J.M. (2006) Model of chromosome motility in Drosophila embryos: Adaptation of a general mechanism for rapid mitosis. Biophysical journal *90*, 3966-3982.

Cole, D.G., Saxton, W.M., Sheehan, K.B., and Scholey, J.M. (1994). A "slow" homotetrameric kinesin-related motor protein purified from Drosophila embryos. The Journal of biological chemistry *269*, 22913-22916.

Cottingham, F.R., Gheber, L., Miller, D.L., and Hoyt, M.A. (1999). Novel roles for saccharomyces cerevisiae mitotic spindle motors. The Journal of cell biology *147*, 335-350.

Cytrynbaum, E.N., Scholey, J.M., and Mogilner, A. (2003). A force balance model of early spindle pole separation in Drosophila embryos. Biophysical journal *84*, 757-769.

Cytrynbaum, E.N., Sommi, P., Brust-Mascher, I., Scholey, J.M., and Mogilner, A. (2005). Early spindle assembly in Drosophila embryos: role of a force balance involving cytoskeletal dynamics and nuclear mechanics. Molecular biology of the cell *16*, 4967-4981.

Danuser, G., and Waterman-Storer, C.M. (2006). Quantitative fluorescent speckle microscopy of cytoskeleton dynamics. Annual review of biophysics and biomolecular structure *35*, 361-387.

Enos, A.P., and Morris, N.R. (1990). Mutation of a gene that encodes a kinesin-like protein blocks nuclear division in A. nidulans. Cell *60*, 1019-1027.

Goshima, G., Wollman, R., Stuurman, N., Scholey, J.M., and Vale, R.D. (2005). Length control of the metaphase spindle. Curr Biol *15*, 1979-1988.

Heck, M.M., Pereira, A., Pesavento, P., Yannoni, Y., Spradling, A.C., and Goldstein, L.S. (1993). The kinesin-like protein KLP61F is essential for mitosis in Drosophila. The Journal of cell biology *123*, 665-679.

Howard, J. (2001). Mechanics of motor proteins and the cytoskeleton (Sunderland, Mass., Sinauer Associates Publishers).

Hoyt, M.A., He, L., Loo, K.K., and Saunders, W.S. (1992). Two Saccharomyces cerevisiae kinesin-related gene products required for mitotic spindle assembly. The Journal of cell biology *118*, 109-120.

Joglekar, A.P., and Hunt, A.J. (2002). A simple, mechanistic model for directional instability during mitotic chromosome movements. Biophysical journal *83*, 42-58.

Kapitein, L.C., Peterman, E.J., Kwok, B.H., Kim, J.H., Kapoor, T.M., and Schmidt, C.F. (2005). The bipolar mitotic kinesin Eg5 moves on both microtubules that it crosslinks. Nature *435*, 114-118.

Marshall, W.F., Marko, J.F., Agard, D.A., and Sedat, J.W. (2001). Chromosome elasticity and mitotic polar ejection force measured in living Drosophila embryos by four-dimensional microscopy-based motion analysis. Current Biology *11*, 569-578.

Mastronarde, D.N., McDonald, K.L., Ding, R., and McIntosh, J.R. (1993). Interpolar spindle microtubules in PTK cells. The Journal of cell biology *123*, 1475-1489.

McDonald, K.L., O'Toole, E.T., Mastronarde, D.N., and McIntosh, J.R. (1992). Kinetochore microtubules in PTK cells. The Journal of cell biology *118*, 369-383.

Mitchell, M. (1996). An introduction to genetic algorithms (Cambridge, Mass., MIT Press).

Rogers, G.C., Rogers, S.L., Schwimmer, T.A., Ems-McClung, S.C., Walczak, C.E., Vale, R.D., Scholey, J.M., and Sharp, D.J. (2004). Two mitotic kinesins cooperate to drive sister chromatid separation during anaphase. Nature *427*, 364-370.

Rogers, G.C., Rogers, S.L., and Sharp, D.J. (2005). Spindle microtubules in flux. Journal of cell science *118*, 1105-1116.

Saunders, W.S., and Hoyt, M.A. (1992). Kinesin-related proteins required for structural integrity of the mitotic spindle. Cell *70*, 451-458.

Sawin, K.E., LeGuellec, K., Philippe, M., and Mitchison, T.J. (1992). Mitotic spindle organization by a plus-end-directed microtubule motor. Nature *359*, 540-543.

Scholey, J., and Mogilner, A. (2002). Mitotic Spindle Motors. In Mitotic Spindle Motors, S. M., ed. (Wiley-VCH), pp. p. 327-355.

Sharp, D.J., Brown, H.M., Kwon, M., Rogers, G.C., Holland, G., and Scholey, J.M. (2000). Functional coordination of three mitotic motors in Drosophila embryos. Molecular biology of the cell *11*, 241-253.

Sharp, D.J., McDonald, K.L., Brown, H.M., Matthies, H.J., Walczak, C., Vale, R.D., Mitchison, T.J., and Scholey, J.M. (1999). The bipolar kinesin, KLP61F, cross-links microtubules within interpolar microtubule bundles of Drosophila embryonic mitotic spindles. The Journal of cell biology *144*, 125-138.

Straight, A.F., Sedat, J.W., and Murray, A.W. (1998). Time-lapse microscopy reveals unique roles for kinesins during anaphase in budding yeast. The Journal of cell biology *143*, 687-694.

Tao, L., Mogilner, A., Civelekoglu-Scholey, G., Wollman, R., Evans, J., Stahlberg, H., and Scholey, J.M. (2006). A homotetrameric kinesin-5, KLP61F, bundles microtubules and antagonizes Ncd in motility assays. Curr Biol *16*, 2293-2302.

Tawada, K., and Sekimoto, K. (1991). Protein friction exerted by motor enzymes through a weak-binding interaction. Journal of theoretical biology *150*, 193-200.

Topchy, A.P., Law, M.H.C., Jain, A.K., and Fred, A.L. (2004). Analysis of consensus partition in cluster ensemble. Proceedings of the Fourth IEEE International Conference on Data Mining 225-232

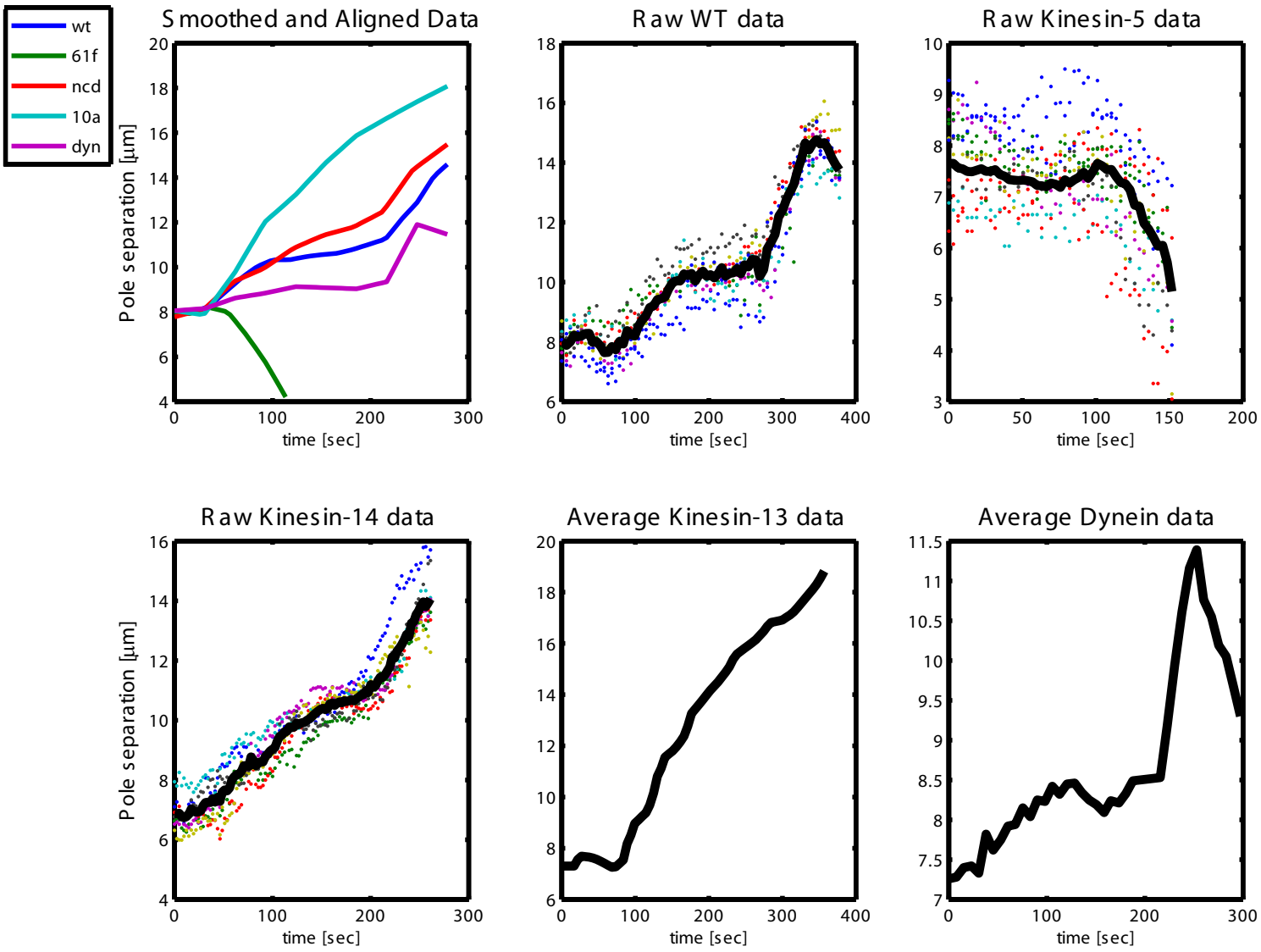

Supplementary figure 1. **Raw data**

The experimental data used for this study is shown. Upper left corner is the data after it has been processed and is the same as main Fig. 1c. The other panels shows the raw data for each of the 5 datasets used, dots representing single spindle data (each color - a different spindle), and black lines are the dots averages. For Kinesin-14 and Dynein, single spindle measurements were not available and only the averages are shown.

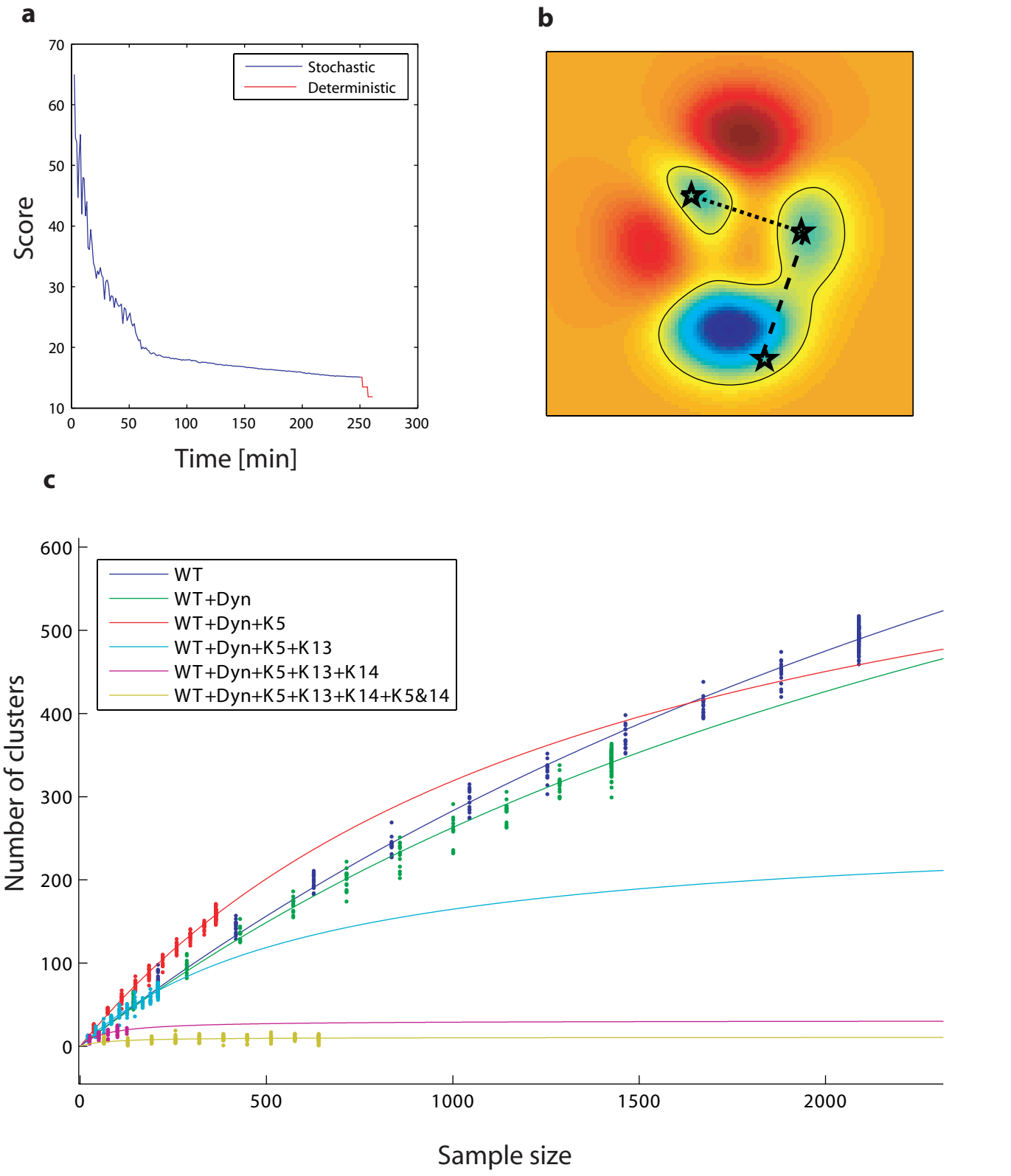

Supplementary figure 2: **Optimization and clustering.**
a A sample optimization run. Evolution of the optimization scores as a function of CPU time. A single optimization required ~4 CPU hours. Blue line is the stochastic optimization and the red line is the deterministic improvement that follows. b An illustration of the clustering criterion. The color codes a hypothetic two-dimensional fitness landscape. Three points in this space represent identified models. The dotted line shows a pair of models that will generate 'nonviable progeny' models that are not good fits for the data. The dashed line shows a pair of models that generate 'viable progenies' - all points along the dashed line generate models that are a good fit to the experimental data. To determine if a set of models is indeed a group, 1000 new models are generated as a mixture of the models in that set. That set is identified as a cluster if more than half of the pairs are 'viable'. c Convergence analysis of the six search iterations. As the sample size increases, the number of identified model clusters increases in a hyperbolic fashion.

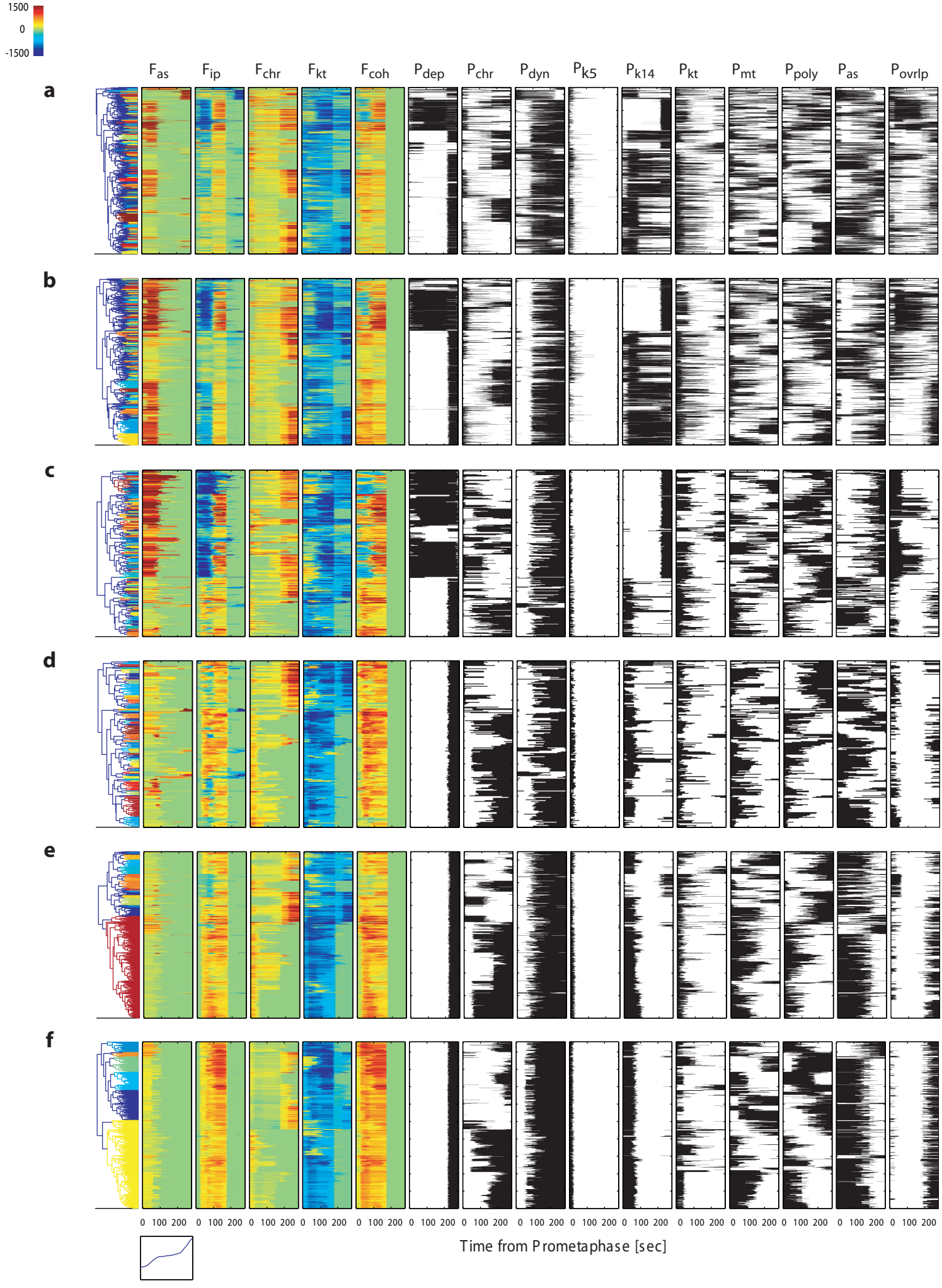
1500
0
-1500
Fas
Fip
Fchr
Fkt
Fcoh
Pdep
Pchr
Pdyn
Pk5
Pk14
Pkt
Pmt
Ppoly
Pas
Povrlp
a
b
c
d
e
f
0 100 200
Time from Prometaphase [sec]

Supplementary figure 3. Search results

This figure shows the results of the cluster analysis for models that fit all available experimental data for all six iterations of the search. Dendrogram shows the hierarchical tree of all models. The identified clusters within the tree are color-coded. Time series for the forces on the four MT populations and cohesion forces from prometaphase (t=0) till the end of anaphase B (t=278 s) follow immediately below the dendrogram. Each imaginary vertical line across the panel corresponds to a specific model fitting all available experimental data. The forces (in pN) are color coded according to the bar shown at the upper left corner. For the reference, the time series for the pole-pole distance are shown at the bottom of the figure. Time series for ten motor switches' activity follow immediately below the force time series. White and black correspond to active and inactive motors, respectively. The switches are: P_{dep} – pole depolymerizer; P_{chr} – chromokinesin; P_{dyn} – dynein; P_{k5} – Kinesin-5 sliding motor; P_{k14} – Kinesin-14; P P_{kt} – combined kt motors; P_{mt} – MT plus end depolymerization activity at the kinetochore; P_{poly} – MT plus end polymerization activity at the kinetochore; P_{as} – switch regulating the number of astral MTs; P_{ovrlp} – switch regulating the number of MT at the overlap zone at the spindle equator. The six iteration shown are **a** WT **b** WT and Dynein **c** WT, Dynein and Kinesin-5, **d** WT, Dynein, Kinesin-5 and Kinesin-13. **e** WT, Kinein-5 Kinesin-13 and Kinesin-14 **f** WT, Kinein-5 Kinesin-13, Kinesin-14, and double inhibition of Kinesin-5 and Kinesin-14.

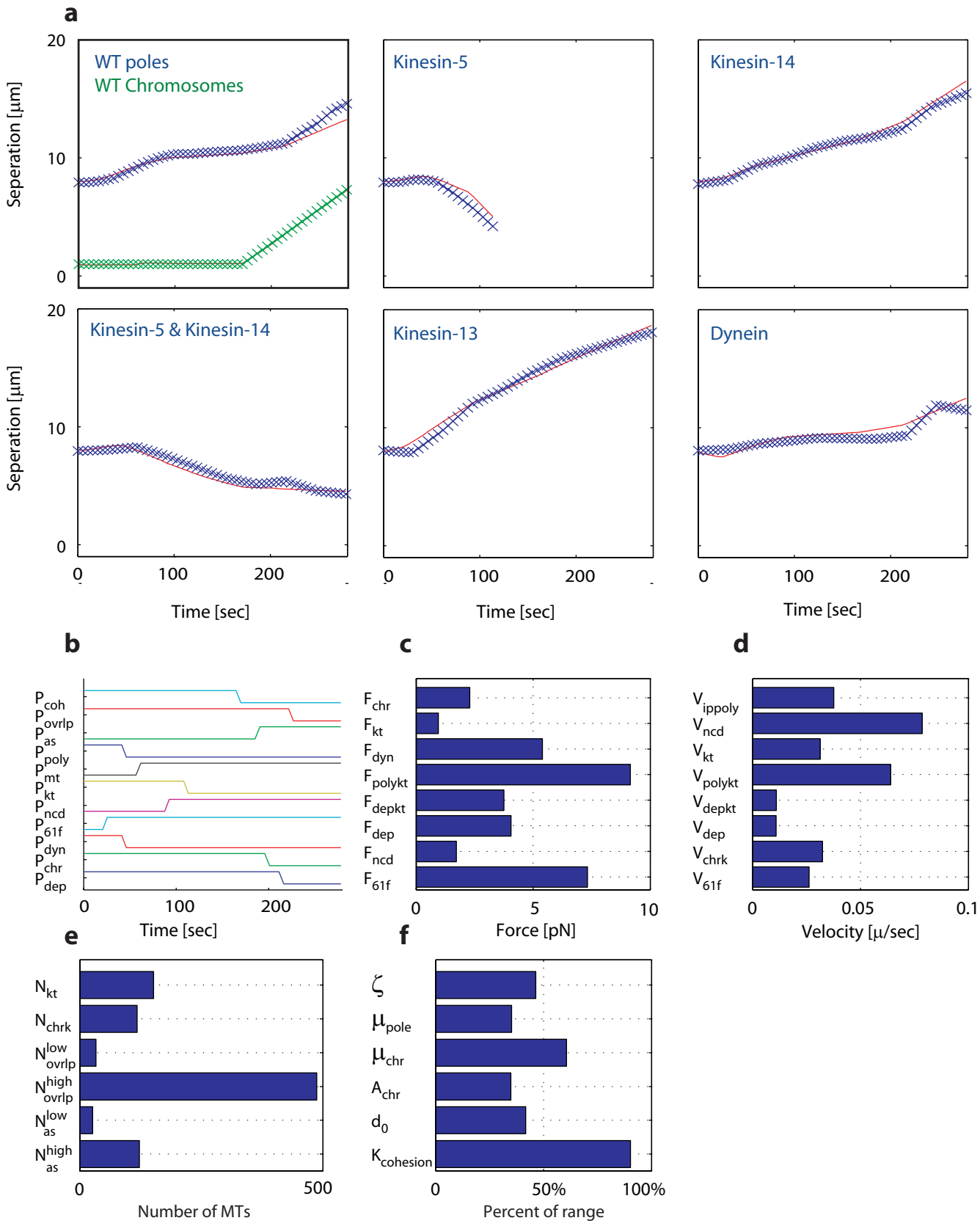

Supplementary figure 4. **Example of a successful model**
The same model that is shown in Fig. 5 is shown here. The fit for the different experimental datasets (a) is shown. The pole separation data is shown in blue, chromosome separation in green and the simulation results, in both cases, in red. The profiles of the 10 switches are shown in b. The remaining 34 parameters are shown in panels c-g. Panel c-f shows actual parameter values, whereas panel g shows the percent of the allowed range that is shown in supplementary table 1.

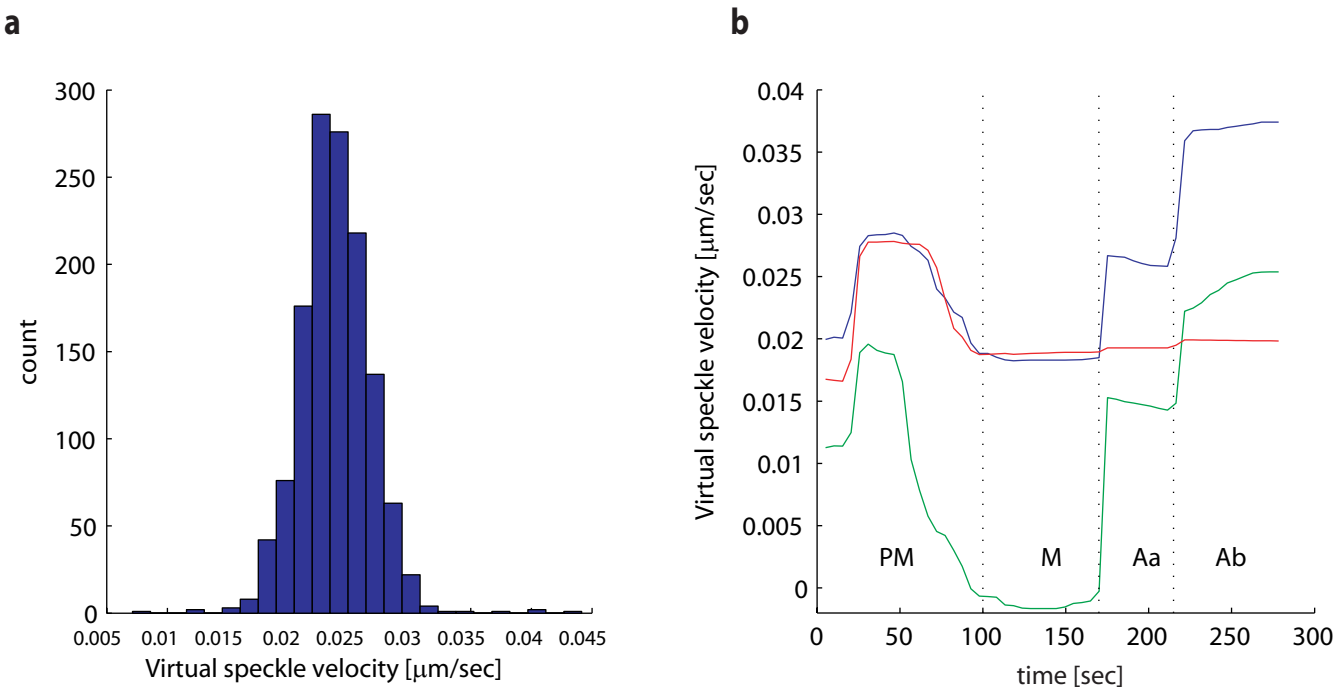

Supplementary figure 5. **Virtual speckle (flux) analysis**
The average speckle velocity that is predicted by the models was conserved among all models. a: The distribution of the median speckle velocity. b: The average MT velocity is a weighted average of the three MT populations taking into account the relative number of MTs from each population.

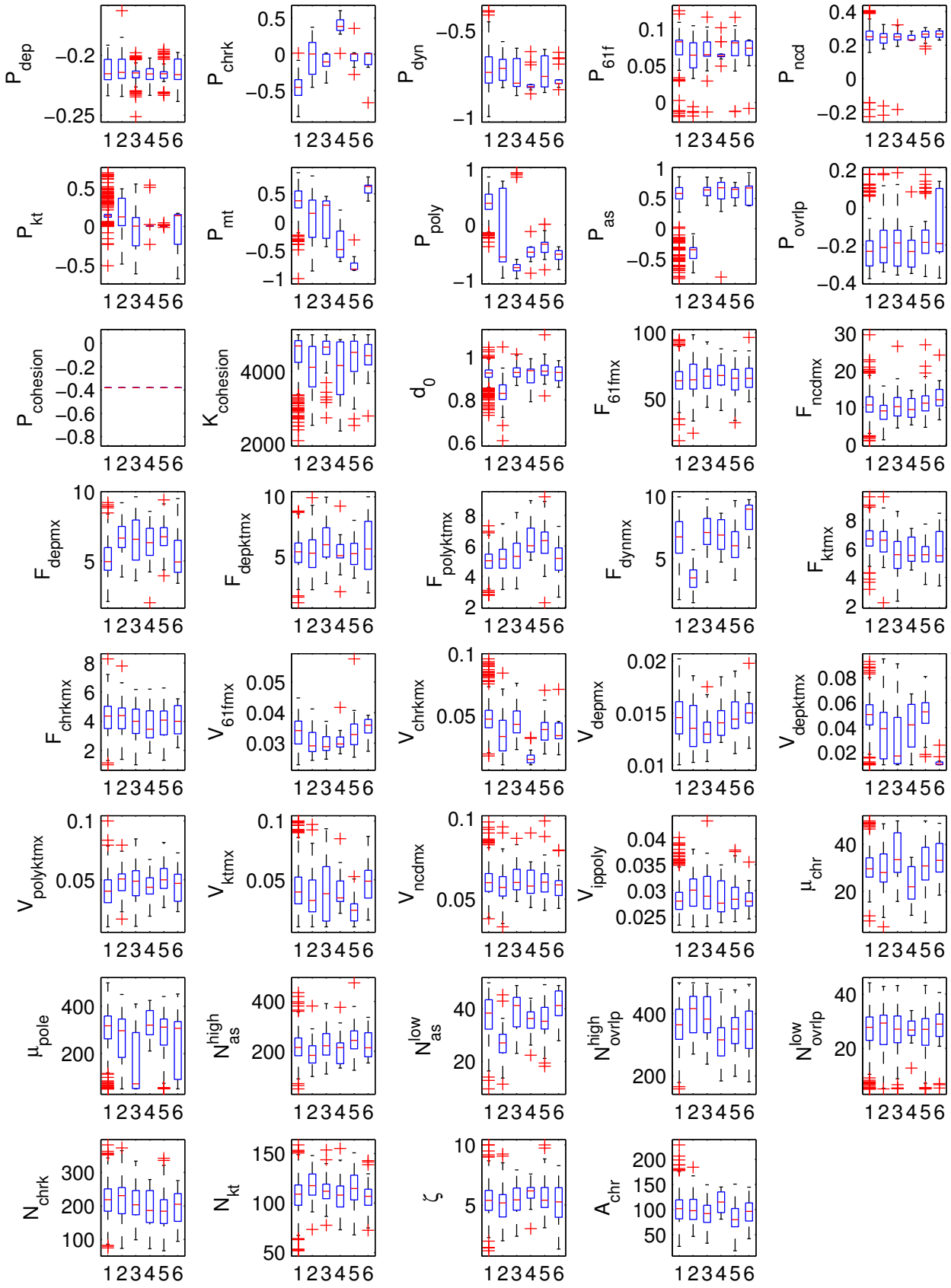
P_dep
P_chrk
P_dyn
P_61f
P_ncd
P_kt
P_mt
P_poly
P_as
P_ovrlp
P_cohesion
K_cohesion
d_0
F_61fmx
F_ncdmx
F_depmx
F_depktmx
F_polyktmx
F_dynmx
F_ktmx
F_chrkmx
V_61fmx
V_chrkmx
V_depmx
V_depktmx
V_polyktmx
V_ktmx
V_ncdmx
V_ippoly
μ_chr
μ_pole
N_as^high
N_as^low
N_ovrlp^high
N_ovrlp^low
N_chrk
N_kt
ζ
A_chr
1 2 3 4 5 6

Molecular Systems Biology 4; Article number 194; doi:10.1038/msb.2008.33
Citation: *Molecular Systems Biology* 4:194

www.molecularsystemsbiology.com

molecular systems biology

NEWS AND VIEWS

A theoretical model of mitotic spindle elongation under experimental constraints

Thomas Surrey*

European Molecular Biology Laboratory, Cell Biology and Biophysics Unit, Heidelberg, Germany
* Corresponding author. European Molecular Biology Laboratory, Meyerhofstrasse 1, Heidelberg 69117, Germany.
Tel.: +49 6221 387 360; E-mail: surrey@embl.de
Molecular Systems Biology 6 May 2008; doi:10.1038/msb.2008.33

During the division of eukaryotic cells, the duplicated set of chromosomes is separated by the mitotic spindle, a large multicomponent assembly consisting of several hundred proteins in human cells (Sauer *et al*, 2005). Researchers have started to move from putting together the parts list of spindle components and from generating an atlas of their localizations toward trying to understand at a systems level the dynamic interplay between these components that ultimately translates into spindle function. This requires, in part, shifting the focus from biochemistry to mechanics. It is clear now that the mechanical properties of microtubules and molecular motors are crucial for spindle structure and function. But how they work together is still a mystery and there is a need for modeling this interplay, because our intuition reaches its limits when trying to understand it. The paper by Wollman *et al* (2008) in this issue reports on the next step of the development of a model that allows one to describe one aspect of spindle behavior for which good quantitative experimental data exist, namely spindle elongation during the period between prophase and anaphase B in *Drosophila* embryos. As their model is based on the mechanical properties of major elements of the spindle, the quantitative comparison with available data allows the authors to make predictions about how the concerted action of the different mechanical elements leads to spindle elongation.

Among others, there are two major challenges when trying to model the spindle (Karsenti *et al*, 2006). (1) What is the right level of description? This means what is the minimal set of molecular activities that needs to be considered and how much detail needs to be included in the model to have a chance of a rather close description of reality by the model? (2) What are the actual values of the parameters chosen to describe the properties of the molecular players considered in the model? In the ideal case, one would simply measure these parameter values experimentally and then use them for the model to see if it recapitulates the experimental measurement.

Wollman *et al* addressed these two challenges in the following manner. They chose a one-dimensional representation of the spindle as the basis of their model, as spindle elongation is essentially a one-dimensional problem. They assumed a pre-existing geometry of interconnected spindle components such as chromosomes, spindle poles, microtubules and motors that can vary in their exact configuration. They differentiated between different microtubule populations such as astral microtubules connecting the spindle poles to the cortex, microtubules connecting the spindle poles either to kinetochores or to chromosome arms and microtubules extending from opposite poles toward the spindle center where they overlap. Different motor populations localized to the cortex, kinetochores, chromosome arms or to the antiparallel microtubule overlap and regulated microtubule dynamics produce forces by acting selectively on one or the other microtubule population. The authors calculated the variation in spindle length from the sum of all forces produced by the different populations of the mechanical elements considered in their model. Variations in motor activity, microtubule dynamics or number of microtubules were represented by binary switches that change enzyme activity or microtubule number in a step-like manner during spindle elongation. In summary, the authors constructed a fully deterministic model for spindle elongation expressed as a system of ordinary differential equations with around 40 parameters.

Although the model contains strong simplifications, its total parameter value space is still enormous. Because it is not obvious how to solve the system of differential equations analytically, the full range of model behaviors cannot be grasped easily. Wollman *et al* therefore performed a massive screen of a very large range of parameter value combinations, an approach similar to a recent *in silico* screen of a pair of interacting microtubule asters (Nedelec, 2002). The system of differential equations for each parameter value combination was solved numerically and its output of spindle lengths was compared quantitatively with experimental data measured in *Drosophila* embryos, in spirit similar to an approach of another previous study where a theoretical model for kinetochore movements was quantitatively fit to experimental data of budding yeast spindles (Gardner *et al*, 2005).

The authors obtained a very large set of model variants that could reproduce spindle elongation in wild-type *Drosophila* embryos. Interestingly, and to a certain extent also expectedly, the number of model variants producing realistic behavior was significantly reduced when more experimental results from mutants were used as constraints (despite even an increase in the number of parameters in the model). Optimization strategies and cluster analysis boiled down the result to six distinct molecular scenarios potentially underlying spindle elongation, each scenario comprising several slightly different model variants perhaps reflecting a certain robustness of the scenarios. A major outcome was that certain features were shared between all identified scenarios suggesting core

characteristics of spindle functioning that are conserved. The analysis showed that outward forces originating from motors pushing on interpolar microtubules in the spindle center (in early prophase assisted also by forces of motors at the cortex pulling on astral microtubules) are largely balanced by inward kinetochore microtubule forces. Active microtubule depolymerization at the poles counteracted spindle elongation promoted by the outward-pushing motors in the spindle center. This depolymerization stops at the onset of anaphase B when the spindle elongates.

Although the number of possible scenarios could be gradually decreased considerably by successively adding more and more experimental constraints, this study has not yet identified the 'ultimate' scenario for *Drosophila* spindle elongation. It will be interesting to see if considering further experimental results in the future will narrow down the number of scenarios finally to one, representing the 'ultimate' model, or if it will drop even to below one, necessitating modification of the model. In the latter case, a critical evaluation of the assumptions inherent to the model would be required.

Despite the considerable number of model parameters, plausible, yet drastic simplifications had to be made to keep the model manageable. For example, a choice had to be made for the minimal set of essential spindle components required for the process under study. Furthermore, linear force–velocity relationships were used for entire populations of motors, although one expects theoretically that collective motor behavior is nonlinear (Klumpp and Lipowsky, 2005; Campas *et al*, 2006). Other examples for simplifications are the binary nature of the activity and number switches, simplified treatment of biochemical equilibria (no saturation) or the exclusion of the possibility of local concentration variations along the spindle axis. Finally, the deterministic nature of the model neglects any stochasticity that might be inherent to the real functioning of the spindle.

Continued development of modeling approaches such as the one chosen by Wollman *et al* and of alternative approaches with different degrees of coarse-graining as chosen by other researchers (Nedelec, 2002; Gardner *et al*, 2005; Goshima *et al*, 2005; Pecreaux *et al*, 2006; Schaffner and Jose, 2006; Burbank *et al*, 2007; Kozlowski *et al*, 2007) promises to move this field forward, especially if combined with experimental measurements of crucial parameter values identified by the modeling.

Two lines of experimental research will most likely be important in the future: gathering more quantitative information about the detailed dynamics of the key mechanical elements of the spindle as measured directly inside intact spindles. These experimental data will serve as a reference for the quantitative evaluation of the output produced by different models. Furthermore, it will be important to verify some of the key assumptions going into the modeling in well-defined systems by biochemical reconstitution approaches aiming at building more complex, functional subelements of the microtubule cytoskeleton from purified components *in vitro*. Such well-controlled *in vitro* systems have the charm of offering the possibility of having a rather complete knowledge of most of the parameter values relevant for the description of the system and provide therefore a rather direct test for the validity of the choice of simplifying assumptions going into the modeling (Surrey *et al*, 2001). Despite still some skepticism among some researchers regarding the feasibility of such engineering approaches, either in the test tube or in the computer, they have the potential for finally leading us to understand three-dimensional spindle morphogenesis and spindle function based on the physical properties of its components.

References

Burbank KS, Mitchison TJ, Fisher DS (2007) Slide-and-cluster models for spindle assembly. *Curr Biol* **17:** 1373–1383

Campas O, Kafri Y, Zeldovich KB, Casademunt J, Joanny JF (2006) Collective dynamics of interacting molecular motors. *Phys Rev Lett* **97:** 038101

Gardner MK, Pearson CG, Sprague BL, Zarzar TR, Bloom K, Salmon ED, Odde DJ (2005) Tension-dependent regulation of microtubule dynamics at kinetochores can explain metaphase congression in yeast. *Mol Biol Cell* **16:** 3764–3775

Goshima G, Wollman R, Stuurman N, Scholey JM, Vale RD (2005) Length control of the metaphase spindle. *Curr Biol* **15:** 1979–1988

Karsenti E, Nedelec F, Surrey T (2006) Modelling microtubule patterns. *Nat Cell Biol* **8:** 1204–1211

Klumpp S, Lipowsky R (2005) Cooperative cargo transport by several molecular motors. *Proc Natl Acad Sci USA* **102:** 17284–17289

Kozlowski C, Srayko M, Nedelec F (2007) Cortical microtubule contacts position the spindle in *C. elegans* embryos. *Cell* **129:** 499–510

Nedelec F (2002) Computer simulations reveal motor properties generating stable antiparallel microtubule interactions. *J Cell Biol* **158:** 1005–1015

Pecreaux J, Roper JC, Kruse K, Julicher F, Hyman AA, Grill SW, Howard J (2006) Spindle oscillations during asymmetric cell division require a threshold number of active cortical force generators. *Curr Biol* **16:** 2111–2122

Sauer G, Korner R, Hanisch A, Ries A, Nigg EA, Sillje HH (2005) Proteome analysis of the human mitotic spindle. *Mol Cell Proteomics* **4:** 35–43

Schaffner SC, Jose JV (2006) Biophysical model of self-organized spindle formation patterns without centrosomes and kinetochores. *Proc Natl Acad Sci USA* **103:** 11166–11171

Surrey T, Nedelec F, Leibler S, Karsenti E (2001) Physical properties determining self-organization of motors and microtubules. *Science* **292:** 1167–1171

Wollman R, Civelekoglu-Scholey G, Scholey JM, Mogilner A (2008) Reverse engineering of force integration during mitosis in the *Drosophila* embryo. *Mol Syst Biol* **4**, (this issue)